



## The May 15, 2020 M 6.5 Monte Cristo Range, Nevada, earthquake: eyes in the sky, boots on the ground, and a chance for students to learn

Taha Sadeghi Chorsi, Jochen Braunmiller, Fanghui Deng, Nicholas Mueller, Scott Kerstetter, Robert J. Stern & Timothy H. Dixon

**To cite this article:** Taha Sadeghi Chorsi, Jochen Braunmiller, Fanghui Deng, Nicholas Mueller, Scott Kerstetter, Robert J. Stern & Timothy H. Dixon (2022) The May 15, 2020 M 6.5 Monte Cristo Range, Nevada, earthquake: eyes in the sky, boots on the ground, and a chance for students to learn, International Geology Review, 64:19, 2683-2702, DOI: [10.1080/00206814.2021.2000507](https://doi.org/10.1080/00206814.2021.2000507)

**To link to this article:** <https://doi.org/10.1080/00206814.2021.2000507>



© 2021 The Author(s). Published by Informa UK Limited, trading as Taylor & Francis Group.



[View supplementary material](#)



Published online: 28 Nov 2021.



[Submit your article to this journal](#)



Article views: 2801



[View related articles](#)










[View Crossmark data](#)



Citing articles: 2 [View citing articles](#)

# The May 15, 2020 M 6.5 Monte Cristo Range, Nevada, earthquake: eyes in the sky, boots on the ground, and a chance for students to learn

Taha Sadeghi Chorsi <sup>a</sup>, Jochen Braunmiller <sup>a</sup>, Fanghui Deng <sup>b</sup>, Nicholas Mueller <sup>c</sup>, Scott Kerstetter <sup>d</sup>, Robert J. Stern <sup>c</sup> and Timothy H. Dixon <sup>a</sup>

<sup>a</sup>School of Geosciences, University of South Florida, Tampa, FL, USA; <sup>b</sup>Scripps Institution of Oceanography, University of California, San Diego, CA, USA; <sup>c</sup>Department of Geoscience, University of Texas at Dallas, Richardson, TX, USA; <sup>d</sup>Pioneer Natural Resources Company, Irving, TX, USA

## ABSTRACT

The M 6.5 earthquake that occurred in the Monte Cristo Range near Mina, Nevada on 15 May 2020 was exceptionally well-recorded with both seismic and geodetic instrumentation. The arid nature of the region also facilitated detailed ground mapping of the surface rupture. Here we integrate several independent data sets to illustrate the educational and research opportunities afforded by these rich data sets. We construct a series of models for slip at depth that are consistent with the satellite-derived geodetic data, the distribution of aftershocks, and the mapped surface rupture. We also show that the modelled depth of maximum slip is in good agreement with heat flow and laboratory data on quartz rheology defining the depth of the brittle-ductile transition. The Monte Cristo Range earthquake also suggests new approaches to seismic hazard assessment may be required for earthquakes in rapidly evolving tectonic regions such as the Walker Lane and Eastern California shear zone.

## ARTICLE HISTORY

Received 21 June 2021  
Accepted 25 October 2021

## KEYWORDS

Monte Cristo Range earthquake; Nevada; integrated geologic and geophysical studies; seismic hazard assessment

## 1. Introduction

On 15 May 2020, a magnitude M 6.5 earthquake struck western Nevada approximately 55 km west of the city of Tonopah, near the California-Nevada border. While widely felt across Nevada, central California, and southern Utah, the earthquake caused only moderate damage and no fatalities, reflecting its remote location. The event was exceptionally well recorded by modern seismological and geodetic instrumentation, allowing a detailed geophysical description, and occurred in a well exposed and well-mapped region, giving geological context. Here we review this earthquake from both geophysical and geological perspectives, focusing on how the integration of various data types can be used to better understand what at first glance seemed to be an anomalous geophysical event. We first outline the geologic and geophysical background, then present the seismicity and the geodetic data, and finally present the results of deformation modelling. Supplementary documentation gives more detailed background to some of the concepts, including detailed descriptions of the various techniques we used to investigate the event and links to relevant software. We include worked examples for our data analysis tools and models. Our review is aimed primarily at beginning graduate students and senior


undergraduates but may also be useful to scientists in other fields and to university educators teaching about active tectonics, seismology, geodesy and natural hazards. For more technical studies of the event the reader is referred to Koehler *et al.* (2021) for surface offset data, Zheng *et al.* (2020) for seismic and satellite radar analysis, Ruhl *et al.* (2021) for detailed seismicity analysis, and Hammond *et al.* (2021) for GPS analysis.

## 2. Background

Roughly twenty-five percent of the relative motion between the Pacific and North American plates within the western Great Basin occurs in a zone of transtensional shear that accommodates displacement between the northwest-translating Sierra Nevada block and the west-northwest extending Basin and Range (Figure 1(a)) (Argus and Gordon 1991; Dixon *et al.* 1995, 2000; Miller *et al.* 2001; Oldow *et al.* 2001; Oldow 2003; Bennett *et al.* 2003). Within this zone a complex array of transform and normal faults constitute the Eastern California Shear Zone (ECSZ) and Walker Lane (Figure 1; Dokka and Travis 1990a, Dokka and Travis 1990b; Miller *et al.* 2001; Locke *et al.* 1940; Stewart 1988; Oldow and Craig 1992; Wesnousky 2005a, Wesnousky 2005b; Dickinson 2002).

**CONTACT** Taha Sadeghi Chorsi  [taha4@usf.edu](mailto:taha4@usf.edu)  School of Geosciences, University of South Florida, 4202 E. Fowler Avenue, 33620, Tampa, FL, USA

This article has been republished with minor changes. These changes do not impact the academic content of the article.

 Supplemental data for this article can be accessed [here](#).

© 2021 The Author(s). Published by Informa UK Limited, trading as Taylor & Francis Group.

This is an Open Access article distributed under the terms of the Creative Commons Attribution-NonCommercial-NoDerivatives License (<http://creativecommons.org/licenses/by-nc-nd/4.0/>), which permits non-commercial re-use, distribution, and reproduction in any medium, provided the original work is properly cited, and is not altered, transformed, or built upon in any way.

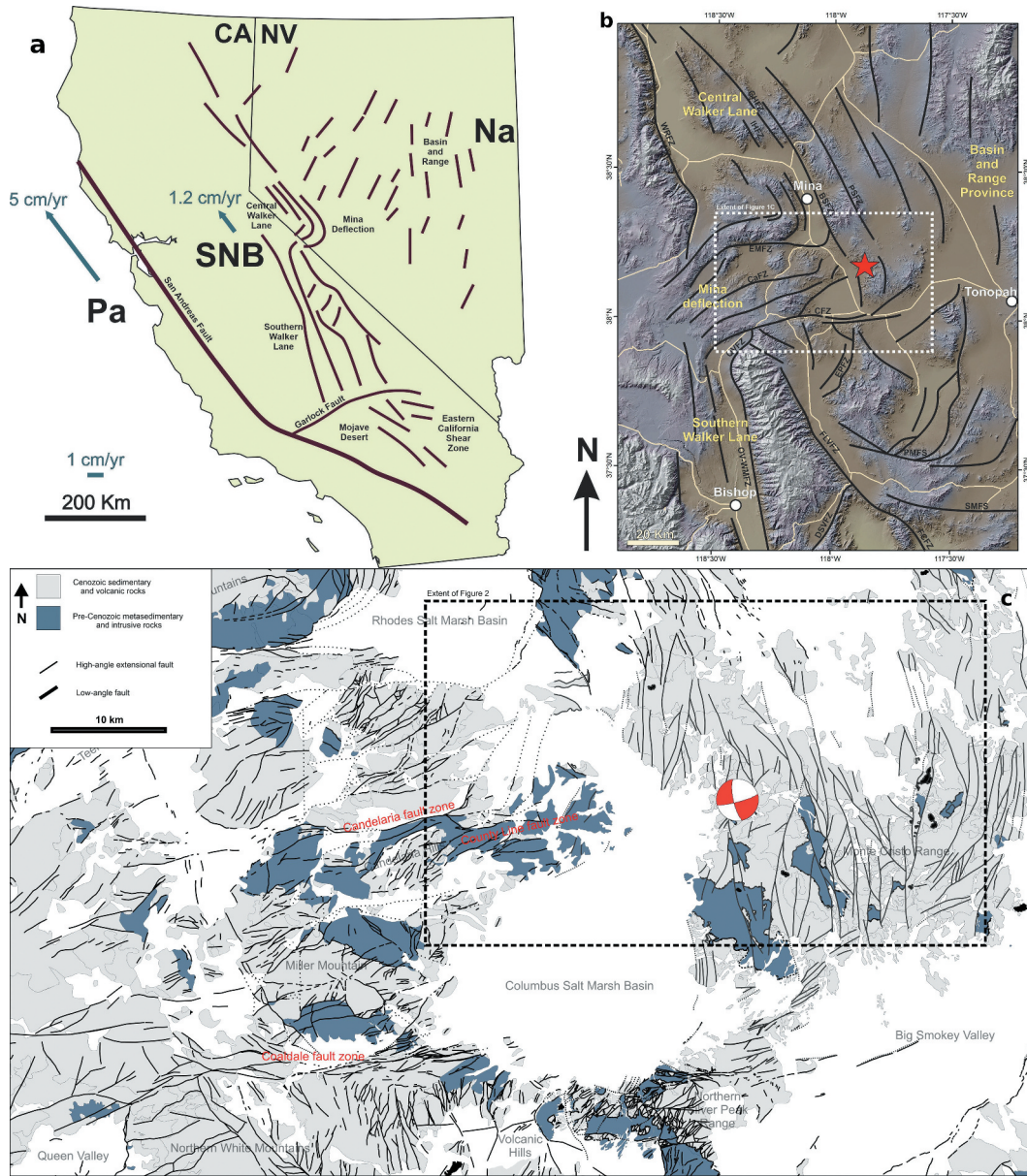


**Figure 1.** (a) Cartoon depicting simplified tectonic elements of western North America. Red lines are late Cenozoic high-angle faults. Blue arrows represent geodetically determined plate motion velocity vectors of the Pacific plate and the Sierra Nevada block relative to North America. Ca – California; Na – North American Plate; NV – Nevada; Pa – Pacific Plate; SNB – Sierra Nevada Block. (b) Shaded relief map of the Mina Deflection region with simplified faults shown as black lines. Tectonic domains are labelled in yellow; names of cities/towns shown in white; red star is location of 15 May 2020 Monte Cristo Range earthquake. Northwest-striking right-oblique faults of the southern and central Walker Lane are kinematically linked by east-northeast-striking left-oblique faults of the Mina Deflection. Extent of Figure 1c shown in dashed white box. BSFZ – Benton Springs fault zone; CaFS – Candelaria fault zone; CFS – Coaldale fault zone; DSVFZ – Deep Springs Valley fault zone; EMFZ – Excelsior Mountains fault zone; EPFZ – Emigrant Peak fault zone; FCFZ – Furnace Creek fault zone; FLVFZ – Fish Lake Valley fault zone; GHFZ – Gumdrop Hills fault zone; IHFZ – Indian Hills fault zone; OV-WMFS – Owens Valley-White Mountains fault zone; PMFS – Palmetto Mountains fault system; PSFZ – Petrified Springs fault zone; QVFS – Queen Valley fault zone; SMFS – Sylvania Mountains fault system; WRFZ – Wassuk Range fault zone. (c) Simplified geologic map of the Columbus Salt Marsh region in the southern Mina Deflection. Faults shown in black, modified from Kerstetter (2018) and Oldow and Cland (2018). Physiographic names shown in dark grey, fault zones mentioned in text shown in red. Fault plane solution is at epicentre of the 15 May 2020 earthquake. Extent of Figures, 3, and 5 indicated by the dashed black box.



Many faults in this region are likely active but with long recurrence times, with dextral and sinistral motions on northwest and east-west striking faults, respectively (Rogers *et al.* 1991). Contemporary transtensional deformation is also well documented by Global Navigation Satellite System (GNSS) data (Dixon *et al.* 2000; Miller *et al.* 2001; McClusky *et al.* 2001; Oldow 2003; Murphy *et al.* 2009; Hammond *et al.* 2011).

The Walker Lane system has long been recognized as a zone of major faulting and deformation, although it would take developments in several fields, including plate tectonics, plate motion models, and high-precision geodesy, before its kinematic significance was fully appreciated. The term Walker Lane was first used by Locke *et al.* (1940) to describe a broad zone of faulting east of the Sierra Nevada, but its relation to extensional Basin and Range faulting further to the east and strike-slip motion on the San Andreas fault to the west was not initially clear. For most of the 20th Century, the earthquake record in the Great Basin was dominated by normal faulting events, such as the 1959 Hebgen Lake, Montana (M 7.3) and 1983 Borah Peak, Idaho (M 6.9) events (e.g. Barrientos *et al.* 1987), and the 1915 Pleasant Valley earthquake (M<sub>s</sub> 7.7; Abe 1981). The 1954 Rainbow Mountain – Fairview Peak – Dixie Valley sequence in Central Nevada has been modelled as a triggered normal fault sequence (Hodgkinson *et al.* 1996a, 1996b) although these authors and Doser (1986) point out that several segments active during the sequence are right-oblique faults (see also Caskey *et al.* 1996). The 1932 Cedar Mountain earthquake (M<sub>s</sub> 7.2) also had right-oblique geometry (Bell *et al.* 1999). Geological mapping of surface offsets associated with the 1872 Owens Valley earthquake had demonstrated the importance of dextral (right-lateral) offsets on northwest-striking faults immediately east of the Sierra Nevada (Lubetkin and Clark 1988; Beanland and Clark 1994). However, it took until the 1992 Landers earthquake (Sieh *et al.* 1993), the first well-recorded earthquake east of the San Andreas fault exhibiting predominantly right-lateral motion, that the seismic hazard from strike-slip faulting in the region was fully appreciated.

Minster and Jordan (1984, 1987) had noted a difference between Pacific – North American relative motion defined by their plate motion model (~5 cm/yr) and the known slip rate on the main plate boundary, the San Andreas fault (~3.5 cm/yr). The difference (~1.5 cm/yr) had to be accommodated on additional faults or deforming regions within the plate boundary zone and became known as the San Andreas discrepancy. Strictly

speaking, the discrepancy is a vector difference, but since most of the deformation turns out to be accommodated on faults that are more or less parallel to the San Andreas, considering just the rate is adequate for most purposes. The main exception is several mm/yr of east-west extension across the Basin and Range, most of which probably occurs across the Wasatch fault in Utah (Malservisi *et al.* 2003; Hammond and Thatcher 2004). Later studies showed that the bulk of the San Andreas discrepancy (10–12 mm/yr) is accommodated by a series of northwest-striking right-lateral strike slip faults in the Walker Lane.

Significant right-lateral shear also occurs in the Mojave Desert, south of the Walker Lane, where a similar zone of deformation is referred to as the Eastern California shear zone (ECSZ; Figure 1(a)). Here, the key evidence for right-lateral shear was both geological and geodetic. Dokka and Travis (1990a, 1990b) first recognized a zone of significant post-Miocene right-lateral displacement across the Mojave, coining the term ECSZ. Sauber *et al.* (1986, 1994) used triangulation data to measure the present-day rate of deformation in the Mojave Desert, documenting 10–12 mm/yr of right lateral displacement across the ECSZ. Savage *et al.* (1990) used trilateration data and obtained a similar result. Subsequent geological studies demonstrated that the deformation was accommodated by half a dozen NW to NNW striking right-lateral faults, all showing evidence for Holocene activity and spanning a 100 km wide deforming zone (see Xie *et al.* 2019 and references therein). Dixon *et al.* (1995, 2000) analysed space geodetic data and showed that essentially the same overall rate and style of deformation continued north of the Mojave Desert, across the active left-lateral Garlock fault into the Owens Valley-Death Valley region. Within Owens Valley, the Walker Lane is sometimes referred to as the ECSZ, although most usage now refers to the deforming zone north of the Garlock fault as the Walker Lane, and we follow that convention here. The complex nature of deformation in the Walker Lane and ECSZ may reflect its relative immaturity as an evolving transform fault zone (Faulds *et al.* 2005; see also discussion in Dixon and Xie 2018).

### 2.1. The mina deflection

Given the similarities in both rate and style of deformation, most investigators consider the ECSZ and Walker Lane to play similar kinematic roles, accommodating that part of Pacific-North America plate motion not focused on the San Andreas fault. Curiously, there is no significant offset as the shear zone crosses the left-lateral



Garlock fault (Dixon and Xie 2018 describe a possible model for this). However, northwest-striking right-oblique faults in the southern Walker Lane (e.g. in Owens Valley) are misaligned relative to similar faults to the north, in the central Walker Lane. Since the Middle Miocene the two systems have been kinematically linked by a series of structural stepovers (right-stepping) that accommodate displacement transfer between the two domains (Figure 1(a)) (Oldow and Craig 1992; Oldow *et al.* 1994, 2008, 2009; Wesnousky 2005a). Modern-day displacement transfer between the southern and central Walker Lane has been ongoing since the middle Pliocene, coinciding with the onset of transtensional deformation throughout the region at ~3–5 Ma (Stockli *et al.* 2003; Lee *et al.* 2009; Mahan *et al.* 2009; Walker *et al.* 2014; Bidgoli *et al.* 2015; Mueller 2019), possibly related to the inland jump of the southern portion of the Pacific–North America plate boundary to its current position in the Gulf of California.

Active displacement within the southern Walker Lane is concentrated along the right-oblique Owens Valley – White Mountains (OV-WM) and Furnace Creek – Fish Lake Valley (FC-FLV) fault zones (Figure 1(b)). Geodetic modelling suggests significant right-oblique displacement at this latitude is localized along the Fish Lake Valley fault zone (Reheis and Dixon 1996; Dixon *et al.* 2000). South of Deep Springs Valley, however, the Owens Valley segment accommodates a larger fraction of displacement (e.g. Lee *et al.* 2001; Dixon *et al.* 2003; Kirby *et al.* 2008).

Displacement in the OV-WM and FC-FLV fault zones is largely transferred along east-northeast-striking left-oblique faults (Ryall and Priestly, 1975; Stewart 1988; Oldow and Craig 1992). This 50 km-wide by 75 km-long zone of active transtension connecting the southern and central Walker Lane is known as the Mina Deflection (Oldow and Craig 1992; Oldow 2003; Oldow *et al.* 2008; Ferranti *et al.* 2009). Readers interested in additional details regarding the geology and tectonics of the Walker Lane and Mina Deflection should consult reviews by Stewart (1988) and Wesnousky (2005a).

The Monte Cristo Range, Nevada earthquake is named after its epicentre location within the northwestern stretches of the Monte Cristo Range, along the Columbus Salt Marsh basin's northeastern boundary. The epicentre occurred 30 km to the southeast of the town of Mina (Figure 1b,c).

### 3. Geology of the Monte Cristo Range earthquake

The Columbus Salt Marsh basin (CSMB) and surrounding mountain ranges are located in the southern Mina Deflection (Figure 1(b,c)) and form the backdrop for the

15 May 2020 earthquake. The CSMB has a triangular geometry reaching up to 20 km wide, flanked by the Monte Cristo Range to the east, the Candelaria Hills to the northwest, Miller Mountain to the west, and the Volcanic Hills and northern Silver Peak Range to the south. The mountains and hills surrounding the CSMB are composed of pre-Cenozoic metasedimentary and intrusive rocks unconformably overlain by a Cenozoic succession of volcanic and sedimentary deposits, separated from the basin by a complex array of faults (Figure 1(c)) (Ross 1961; Albers and Stewart 1972; Speed and Cogbill 1979; Stewart 1979; Oldow and Cland 2018). Late Miocene to contemporary rocks range in thickness from 20 to 3600 m and were deposited during the younger phases of extension (Bachman 1978; Stockli *et al.* 2003; Elias 2005; Oldow *et al.* 2009, 2016). Prior to this, Oligocene to Middle Miocene-aged rocks were deposited in and around east-west-trending basins and vary in thickness from 100 to 2000 m. The basins are bounded to the north and south by east-northeast and west-northwest-striking faults and segmented by north-northwest to north-northeast-striking transfer faults as seen in the Candelaria Hills and on Miller Mountain (Speed and Cogbill 1979; Hardyman *et al.* 1991; Kerstetter 2018). Oldow and Cland (2018) give a detailed description of the late Cenozoic geology of the southern Mina Deflection.

High-angle faults striking east-west, east-northeast, and north-northwest surround the CSMB on all sides and separate the basin from the surrounding ranges (Figure 1b,c) (Oldow and Cland 2018). These basin-bounding faults comprise a curvilinear network of structures that originate from an easterly-striking fault zone several kilometres wide in the southwest corner of the basin, forming active scarps in Pliocene volcanics and late Quaternary alluvium (Lee *et al.* 2006). From here, the fault zone bifurcates to the east and northeast, running along the southern and northwestern flanks of the CSMB, respectively, before reconnecting at the northeast corner of the CSMB near the epicentre of the Monte Cristo Range earthquake mainshock (Figure 1b,c).

The east-west to east-northeast striking Coaldale fault zone forms the southern boundary of the CSMB and the Mina Deflection. It consists of multiple strands cutting across older north-south and north-northeast-striking faults exposed in the northern Volcanic Hills and northern Silver Peak Range (Figure 1(c)). In the west, the Coaldale fault zone is well exposed in a zone up to a kilometre wide, producing impressive fault scarps in Pliocene basaltic units, offsetting them in a left-oblique sense (Lee *et al.* 2006). Further east, the Coaldale fault zone loses its strong geomorphic expression in the southern CSMB but re-emerges as an east-west striking zone of faults in the northern Silver Peak Range. At its

eastern extent, multiple fault strands splay northward into north-northeast to north-south strikes and extend into the Monte Cristo range. Mapped faults in the Monte Cristo Range strike north-south and north-northwest, extending northward over 15 km through the range and along the western range front, seemingly cutting across the east-northeast trending fault that ruptured at depth during the M 6.5 earthquake. Deformation is widely distributed and spans the entire 22 km width of the range. These active faults dissect an early Miocene-aged low-angle detachment system that structurally juxtaposes Cenozoic volcanic and sedimentary strata with Palaeozoic to Mesozoic rocks (Oldow and Cland 2018).

Along the northwest flank of the CSMB, a northeast-striking fault zone separates the basin from bedrock on Miller Mountain and the Candelaria Hills (Speed and Cogbill 1979; Stewart 1979; Kerstetter 2018). These unnamed faults are discontinuously exposed and express themselves locally as scarps in alluvium and offset outcrops of Quaternary basalt flows (Figure 1(c)). East-northeast and west-northwest-striking faults exposed within Miller Mountain are truncated by the range front fault zone and are also cross-cut by smaller northeast-striking faults within the range. To the northeast, the Candelaria Hills expose a complex series of east-northeast-striking faults, including the Candelaria fault and County Line fault. Together with the northeast-striking range-front fault zone, these faults define a 6–7 km wide zone of active deformation. Recent activity is indicated by left-obliquely offset alluvial deposits and, of course, by the Monte Cristo Range earthquake and its aftershocks.

Within the Mina Deflection, east-west and northwest-striking faults behave as a kinematically coordinated system of curved faults (Ferranti *et al.* 2009). Current extension in the region is oriented about N65°W as documented by GPS, earthquake focal mechanism, and fault-slip data (Oldow 2003; Katopody 2018). Faults within the Mina Deflection striking north-northwest tend to display right-oblique slip, whereas faults that strike east-west to east-northeast are characterized by left-oblique slip. Dip-slip displacement is common along northeast-striking faults (Ferranti *et al.* 2009).

Faults in the study region are long-lived and document a sustained but complex history of deformation. Prior to the onset of contemporary west-northwest directed extension, the region underlying the Mina Deflection underwent periods of north-south extension followed by east-northeast extension during the Oligocene and Miocene (Hardyman *et al.* 1991; Kerstetter 2018; Katopody 2018). This means that within the Mina Deflection, some east-northeast-striking faults

may have originated as dip-slip dominated normal faults that were later reactivated, ultimately expressing themselves as the left-oblique faults we see today.

Fault reactivation may therefore play an important role in the Mina Deflection. Fracture of previously faulted material is presumably favoured from a minimum work standpoint, but the extent of weakening (reduced friction) on such reactivated faults is not clear and may depend on fault healing processes (see Supplement Figure S1).

Surface ruptures associated with the earthquake were mapped by the Nevada Bureau of Mines and Geology (Koehler *et al.* 2021; Dee *et al.* 2021). One of the surprising results is that most ruptures are located well to the west of the earthquake epicentre (Figure 2). The offsets (up to 0.2 m lateral motion) are also small given the expected offset for a M 6.5 earthquake, of order 1 metre (e.g. Wells and Coppersmith 1994). We will show that some of this can be understood when we use geophysical techniques like seismology and geodesy to better describe the sub-surface processes. Photographs of representative offsets and additional discussion are given in the Supplement.

#### 4. Seismological data

The seismological description of the Monte Cristo Range earthquake and its aftershocks uses primary information from the USGS and includes earthquake locations and seismic phase data for event relocations contributed by the Nevada Seismological Laboratory (NSL). Earthquake source mechanisms are from the USGS, NSL, the Global Centroid Moment Tensor project (Ekström *et al.* 2012)

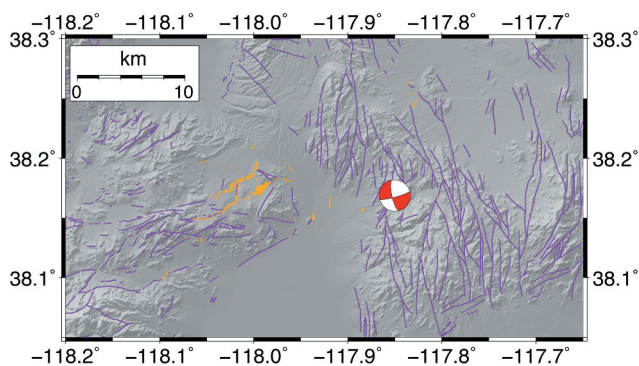


**Figure 2.** Map of the Monte Cristo Range mainshock. The fault plane solution is the Global Centroid Moment Tensor solution (with strike = 76°, dip = 81°, and rake = -16°) for the  $M_w = 6.5$  mainshock centred on the NSL epicentre. The purple lines are (undifferentiated) faults shown in Figure 1(c), as modified from Kerstetter (2018) and Oldow and Cland (2018). The Orange lines are the major surface ruptures and fractures mapped by Dee *et al.* (2021).

and the Saint Louis University (SLU) Moment Tensor Determinations (Herrmann *et al.* 2011) project. We performed relative earthquake relocation and plot the seismicity and focal mechanisms for a seismological interpretation of the sequence. We refer to Ruhl *et al.* (2021) for an in-depth analysis of all aftershocks recorded by the NSL in the first 3.5 months after the main shock. Our analysis covers the 7 months of the sequence up to 15 December 2020.

The Monte Cristo Range earthquake occurred at 11:03:27 UTC on 15 May 2020 (Table 1). With a moment magnitude of  $M_w$  6.5, it is the largest earthquake in Nevada since the 1954 Dixie Valley earthquake sequence (Doser 1986), which was associated with normal and right-oblique faulting northeast of the Walker Lane. The epicentre of the main shock is located within the Monte Cristo Range at 38.169°N and 117.850°W (NSL) consistent with the USGS location which was only about 1 km to the southwest. The surface rupture area is observed 10–15 km west of the epicentre (Figure 2), presumably due to rupture propagation. The hypocentre depth is less well constrained because the closest permanent seismic station is almost 40 km away. This results in low depth sensitivity for first arrival-based locations. The NSL hypocentre depth is 3 km while the USGS depth is 11 km. No foreshocks are reported.

The main shock moment tensor solutions obtained by several groups are similar and indicate a strike-slip source mechanism (Figure 2). Based on the two nodal planes, the active fault could have been a north-north-west trending right-lateral strike-slip fault, consistent with overall expectations for the Walker Lane. However, most mapped faults in the immediate area as well as the distribution of aftershocks indicate that faulting occurred on the other nodal plane, i.e. left-lateral

motion on an east-northeast trending fault. Thus, the earthquake occurred within the Mina Deflection, the major right-step of the Walker Lane. The fault is nearly vertical but likely dips slightly to the south (5–15° relative to vertical) based on the moment tensor solutions. The distribution of re-located aftershocks also indicates a southward dip. The seismic moment from long-period waveform modelling is equivalent to  $M_w$  6.5.

The main shock initiated an intense aftershock sequence with more than 18,000 located earthquakes during the first seven months following the main shock (Figure 3). The recorded aftershocks range in size from

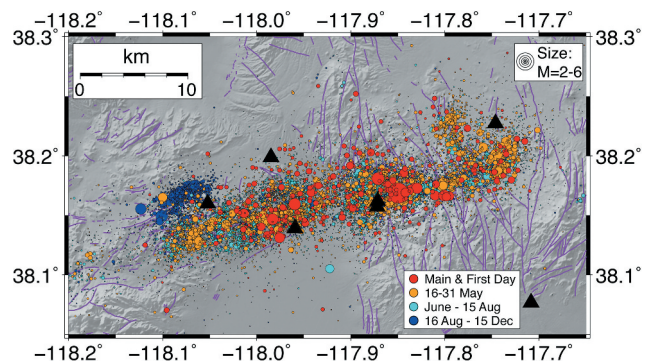


**Figure 3.** Map of 18,724 aftershocks from 15 May to 15 December 2020 ranging in size from  $M_L = 0$  to 5.3. First day aftershocks in red are plotted on top of later aftershocks (Orange, cyan, dark blue are approximately the first 2 weeks, 3 months, and 7 months of aftershocks, respectively) to illustrate regions immediately active; note the cluster of dark blue circles at the western end of the aftershock zone, which became active 1 December. Solid black triangles show temporary seismic stations installed by NSL and USGS; no permanent station is located within the area on the map. The purple lines are (undifferentiated) faults shown in Figure 1(c), as modified from Kerstetter (2018) and Oldow and Cland (2018).

**Table 1.** Locations and source mechanisms of the main shock and its 14 largest aftershocks ( $M \geq 4.8$ ). Location, depth (Z), and  $M_L$  are from NSL; source mechanisms and  $M_w$  are from moment tensor analysis with column 'Mec' describing their origin (see text). St, Di, and Ra are strike, dip, and rake of the ~east-west trending nodal plane. 'N/A' means 'not available'.

Date [Yr/Mo/Da]	Time	Lat [°N]	Lon [°W]	Z [km]	$M_L$	$M_w$	St [°]	Di [°]	Ra [°]	Mec
20/05/15	11:03:27	38.169	117.850	2.7	6.5	6.5	75	81	-16	GCMT
20/05/15	11:18:12	38.160	117.960	3.8	4.9	N/A	N/A	N/A	N/A	N/A
20/05/15	11:26:02	38.181	117.871	6.8	5.1	4.8	248	79	-21	USGS
20/05/15	11:52:07	38.147	117.983	5.8	4.8	N/A	N/A	N/A	N/A	N/A
20/05/15	15:23:25	38.167	117.801	7.6	4.8	4.1	95	90	-15	SLU
20/05/20	12:36:53	38.201	117.745	11.7	5.0	4.8	267	69	-16	USGS
20/05/22	00:22:01	38.231	117.794	7.2	5.1	4.7	72	84	-3	USGS
20/06/08	03:24:06	38.206	117.791	5.2	4.8	4.7	64	90	7	USGS
20/06/19	20:42:21	38.170	117.835	6.5	4.9	4.5	102	84	-8	USGS
20/06/30	09:24:24	38.154	117.958	8.3	5.0	4.5	260	89	3	USGS
20/11/13	09:13:52	38.169	117.853	4.8	5.3	5.3	75	74	-16	USGS
20/12/01	23:32:57	38.164	118.084	5.0	5.1	4.9	69	78	-36	USGS
20/12/03	05:15:30	38.175	118.065	5.0	4.9	4.8	77	74	-33	USGS
20/12/12	07:50:53	38.150	118.101	6.4	4.9	4.6	67	65	-31	USGS
20/12/14	21:20:11	38.155	118.123	5.2	4.7	4.8	76	63	-38	USGS



local magnitude  $M_L = 0$  to 5.3. Table 1 lists all 15  $M \geq 4.8$  events until 15 December 2020. The first strong  $M$  5.1 aftershock occurred within 23 minutes of the main shock 2 km to the northwest; the second  $M$  5.1 aftershock occurred almost one week after the main event (on 22 May) and about 10 km to the northeast. The largest aftershock with  $M_L=5.3$  occurred on 13 November, within a few hundred metres of the main shock epicentre. The first station of a temporary seismic network was installed by UNR and USGS scientists within 30 hours of the main shock. The network eventually consisted of 8 temporary seismic stations in the epicentral region, reducing the detection and location threshold from about  $M = 2$  to about  $M = 0$ .

Figure 4 (top) shows the frequency-size distribution (Gutenberg-Richter relation) of the aftershocks. The observations (black circles) are well-fit by a  $b$ -value of  $0.85 \pm 0.01$  obtained from linear regression (red line) of

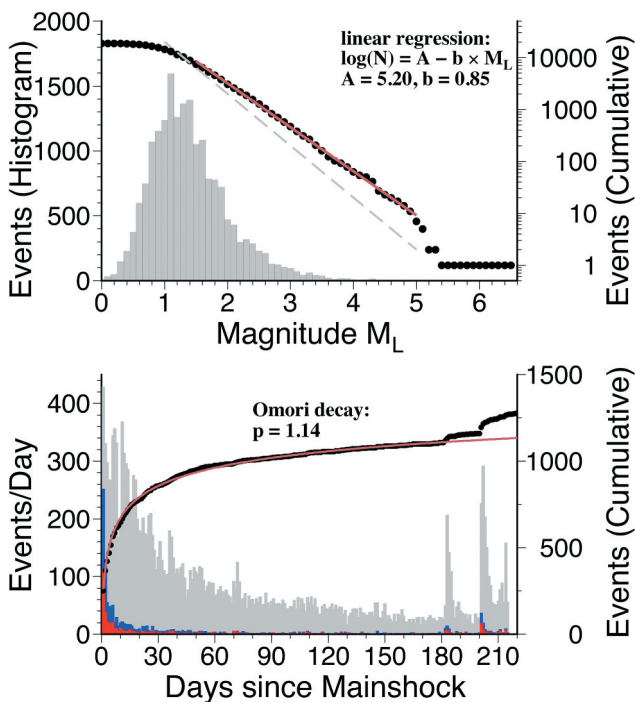


**Figure 4.** Size and temporal distribution of the first seven months of the Monte Cristo Range aftershock sequence. (top) Frequency-size (Gutenberg-Richter) distribution. The histogram shows the number of aftershocks in 0.1 magnitude unit bins. The solid circles show the cumulative number of events equal and above a given magnitude. The red line is the least squares fit of the observations in the  $M_L$  1.5 to 5 range resulting in  $b = 0.85 \pm 0.01$  (same as its maximum likelihood estimate, see Supplement); grey dashed line depicts  $b = 1$  and the actual distribution has a slope of less than 1. (bottom) Aftershocks per day: Histograms; red shows  $M_L \geq 3$ , blue  $M_L \geq 2.5$ , and grey all events in catalogue. The cumulative number of  $M_L \geq 2.5$  aftershocks (solid circles) up to 1 November is fit (red curve) with a decay parameter  $p = 1.14$ ; see text for details.

the number of aftershocks versus  $M_L$ ;  $b = 1$  (grey dashes) is inconsistent with the data. Figure 4 (bottom) shows the number of aftershocks per day (as histograms) from the main shock until 15 December 2020. The decay of activity with time is typical and follows the Omori-Utsu law (Utsu 1961), which expresses the expected number of aftershocks per day. We found a decay parameter  $p = 1.1$  for the Monte Cristo sequence from fitting (red line) the cumulative number of  $M_L \geq 2.5$  earthquakes (black circles) until 1 November to exclude the step-like bumps in the observed distribution of aftershocks. The bumps are caused by strong late aftershocks ( $M_L$  5.3 on 13 November;  $M_L$  5.1 on 1 December), which generated their own aftershock sequences. Our results for  $b$  and  $p$  are consistent with estimates from the initial aftershock sequence given by Liberty *et al.* (2021) and Ruhl *et al.* (2021). Additional information about the Gutenberg-Richter (including the maximum likelihood  $b$  estimate) and Omori-Utsu relations is given in the supplement.

We relocated 1,301 larger aftershocks (mostly  $M_L \geq 2.5$ ) using the HypoDD software (Waldhauser and Ellsworth 2000) to better understand the spatial relation of events relative to each other and to mapped faults. Our dataset includes the main event and aftershocks within seven months of the mainshock. Phase data are available from the USGS (<ftp://hazards.cr.usgs.gov/NEICPDE/isf2.0/>).

The HypoDD relocation tightly constrains the location of events relative to each other but does not improve absolute locations. We estimate that the absolute epicentre uncertainties are on the order of 2–3 km. Our relative location uncertainties for most of our events are probably smaller than 1 km even though we used only catalogue data for relocation. Absolute depths are not well-constrained by relocation and the overall distribution stays close to the starting centroid depth (we show results for a starting centroid depth of 6 km) as observed elsewhere (e.g. Williams *et al.* 2011). The mainshock hypocentre depth ( $5.6 \pm 0.8$  km depth relative to the surface) is one of the less constrained parameters during inversion. The reason for this is not clear; we speculate that the dataset for the mainshock differs significantly from the much smaller aftershocks and its actual depth could be closer to the bottom of the distribution. Relocation focuses the seismicity considerably (Figure 5; supplemental Figure S3 shows relocated events colour-coded by depth) and suggests segmented faulting during the mainshock rupture and subsequent aftershock activity involving nearby adjacent faults, as suggested by Ruhl *et al.* (2021). The aftershock distribution is about 35 km long, with most events occurring between 3 and 14 km beneath the surface. First-day aftershocks cover most of the

distribution and provide a rough proxy for the mainshock rupture dimensions (about  $10\text{--}14 \times 25\text{--}30 \text{ km}^2$ ). These dimensions are consistent with empirical scaling relations for strike-slip earthquakes (e.g. Wells and Coppersmith 1994). Combining seismic moment ( $6.5 \times 10^{18} \text{ Nm}$ ), upper crustal rigidity ( $3 \times 10^{10} \text{ Nm}^{-2}$ ), and faulting dimensions ( $250\text{--}420 \times 10^6 \text{ m}^2$ ) results in an average coseismic slip on the order of  $0.5\text{--}1.0 \text{ m}$  for the main shock. We expand on this in the supplement and show that the main event dominated the seismic moment release.

The sequence includes a significant number of stronger aftershocks for which faulting parameters can be obtained from long-period modelling of three-component regional waveforms. Supplemental Figure S4 shows the double-couple fault plane solutions of the mainshock and of 92  $M_w \geq 3.2$  aftershocks on their HypoDD-relocations. The colour-coding (red: strike-slip, cyan: normal faulting; grey: mix) shows a clear separation into strike slip faulting from about  $118.03^\circ\text{W}$  to  $117.76^\circ\text{W}$  and dominantly normal faulting at the tips of the main

strike slip fault (from  $118.1^\circ\text{W}$  to  $118.0^\circ\text{W}$  and east of  $117.76^\circ\text{W}$ ). Most strike-slip events have an east-northeast trending nodal plane (in most cases likely the fault plane), while the normal faulting events occurred on northeast trending faults. These results are exploited in the geodetic models described below.

Cross-sections of relocated events (Figure 5b–d) combined with the fault plane solutions show that the main shock rupture occurred on a steeply ( $\sim 80^\circ$ ) southward dipping fault consistent with the mainshock moment tensor results. The apparent widening of the aftershock distribution near the mainshock epicentre likely corresponds to a small, right-stepping fault offset and possibly an NNW-trending right-lateral or, as suggested by Ruhl *et al.* (2021), a north-south trending normal fault bounding the Columbus Salt Marsh basin even though a right-step should produce a restraining bend. A likely rupture scenario based on the main event's location is that the mainshock rupture initiated at the western end of the southern segment and propagated towards the east-northeast and,

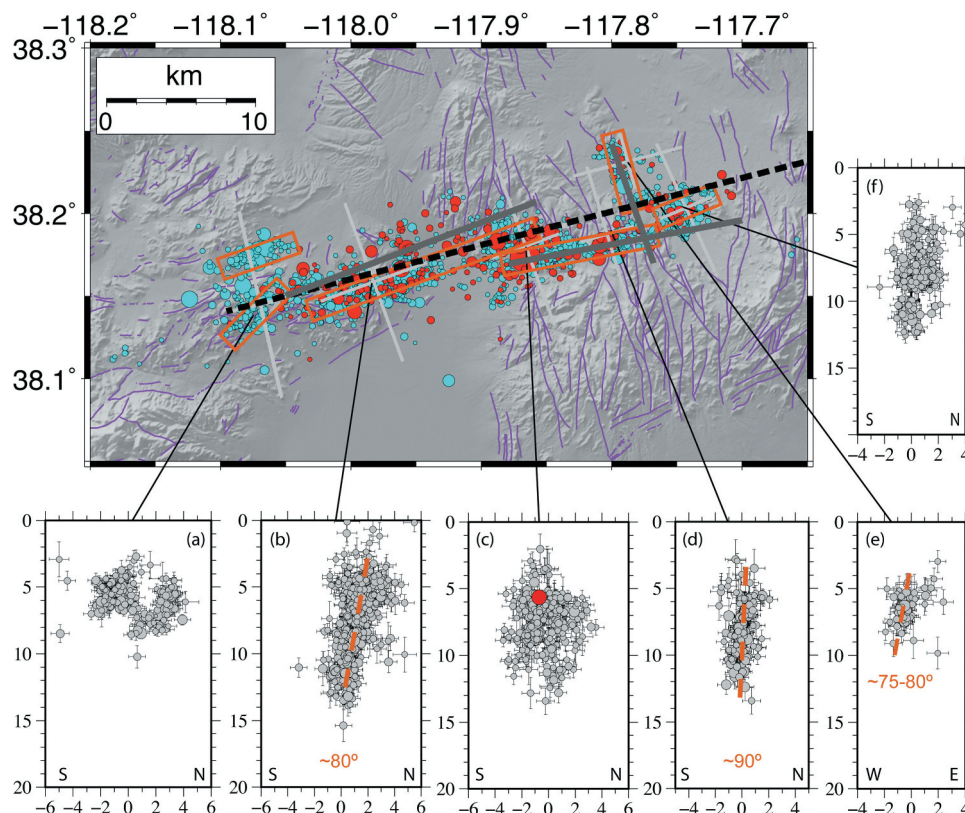


**Figure 5.** Map of mainshock and aftershocks after relative relocation of 1,301 events (mostly  $M_L \geq 2.5$ ). Red are first day, cyan later aftershocks. Orange boxes schematically outline six areas of main activity (see text for details). Gray crosses show cross-section orientations and area of projected events. Thick dashed black and solid grey lines show surface projections of faults used for InSAR modelling; dashed for single fault model; solid for 2- and 3-segment model (NNW-trending segment for latter); see text for details. Cross-sections (a) to (f) point to corresponding map region and have no vertical exaggeration. Red circle in (c) is mainshock. Note absolute depth of event clusters could be changed by a few km up or down; we show results with starting hypocentre depths of 6 km. The purple lines are (undifferentiated) faults shown in Figure 1(c), as modified from Kerstetter (2018) and Oldow and Cland (2018).

possibly due to stress transfer, triggered rupture on the northern, slightly offset (~2 km) segment propagating towards the west-southwest. The west-southwest segment is slightly longer than the eastern rupture and most seismic moment was released along it (see InSAR modelling in Section 6).

A nearly continuous ~10-km-long surface slip with 5–20 cm offset has been observed only along the western segment (mainly west of Highway 95) and mapped by Koehler *et al.* (2021). The surface ruptures are north of most seismicity (corresponding roughly to intense aftershock activity shown in cross-section (b) in Figure 5) consistent with a southward dip of the fault. The apparent offset between the surface ruptures and seismicity in map view indicates that the aftershocks illuminate the main fault at depth. Interestingly, the surface slip is confined to the area east of the mapped trace of the Candelaria fault (Koehler *et al.* 2021) suggesting that the earthquake ruptured a previously unmapped eastern extension of the Candelaria fault.

The mainshock rupture appears to involve at least two east-northeast trending segments. The eastern terminus of predominant strike-slip motion near 117.76°W coincides closely with the southern extension of the north-northwest trending (right-lateral) Petrified Springs fault zone, indicating that the Monte Cristo Range earthquake ruptured the easternmost part of the Mina Deflection.

In addition to left-lateral motion, aftershock clusters also show regions of right-lateral and normal faulting, possibly facilitated by small positive changes in Coulomb Failure Stress. The two larger ( $M_w$  4.7) strike-slip aftershocks north of 38.2°N and near 117.8°W (on 22 May and 8 June, Table 1) likely ruptured on a north-northwest trending conjugate, near-vertical right-lateral fault based on seismicity (map and cross-section (e) in Figure 5). This aftershock zone became active immediately following the main shock. There are indications for activity along other NNW trending conjugate faults such as near 117.95°W. From the width of our relocated earthquakes, it seems likely that other faults parallel and conjugate to the main fault also became active. Conjugate faulting and Coulomb Failure Stress are explained in more detail in the Supplement. Briefly, these reflect westward motion of the block north of the main fault plane. Conjugate faulting seems to play an important role for earthquake sequences in the Walker Lane/ECSZ region, for example the 2019 Ridgecrest sequence (e.g. Ross *et al.* 2019).

Aftershock distributions are particularly wide at the eastern and western ends of the fault zone. Both ends include a number of normal faulting events; their distribution in map view may reflect a shallower dip for

these sub-faults. The eastern end – east of the intersection with the north-northwest trending conjugate fault – includes strike-slip and normal faulting earthquakes; the depth distribution (cross-section (f)) is similar to the strike-slip segments (cross-sections (b)-(e) in Figure 5) and the largest event ( $M_w$  4.8) has a strike-slip mechanism (cross-sections with our data are inconclusive whether the fault is east-west or north-south trending) suggesting a mix of strike-slip and normal faulting.

At the western end – west of about 118.05°W and until December – aftershock mechanisms show considerable normal faulting. The largest aftershocks ( $M_w$  4.1) are smaller than elsewhere. Larger events mainly occurred during the first month following the main shock, and the depth distribution of the aftershocks (about 5–6 km; cross-section (a) in Figure 5) is more compact than for other aftershock zones. These aftershocks could represent activity on a releasing bend of a left-lateral strike slip fault zone involving dip-slip-dominated movement on NE to NNE striking faults. The tension (T) axes trend northwest-southeast, similar to the T-axes trends at the adjacent strike-slip segment. A  $M_L$  5.1 strike-slip earthquake on December 1, slightly north of the normal faulting events, generated its own strong aftershock sequence; these are mainly strike-slip events, and the sequence resembles an earthquake swarm (the largest events have similar magnitudes). The event distribution (Figure 5 and cross-section (a)) suggests activity on an east-northeast trending left-lateral fault.

## 5. Geodetic data

Beginning in the early 1990s, satellite geodetic data began to revolutionize the study of earthquakes by accurately measuring plate motion, inter-seismic strain accumulation and co-seismic and post-seismic strain release. One technique involves the use of ground receivers that measure surface displacement with signals from the Global Positioning System (GPS), now referred to as the Global Navigation Satellite System (GNSS) (Dixon 1991; Bock and Melgar 2016). Hammond *et al.* (2021) describe GPS results for the Monte Cristo Range earthquake, showing how these data provide detailed and unique information on the event. They conclude that the fault slip is of order ~1 m, much greater than the observed < 20 cm surface slip.

Satellite-based Interferometric Synthetic Aperture Radar (InSAR) is the other major satellite geodetic technique used for earthquake studies. The technique was first demonstrated by Gabriel *et al.* (1989) and used by Massonnet *et al.* (1993) to measure surface deformation associated with the 1992 Landers earthquake on one of the active ECSZ faults in the Mojave Desert. Since that



time, InSAR has been used to study earthquakes, active volcanoes, subsidence associated with fluid withdrawal (ground water, oil, and natural gas), landslides, and other crustal motion processes. Briefly, the technique involves illuminating the ground with coherent radar signals and recording both the amplitude and phase of the reflected signal. A subsequent satellite pass (in our case, 2 days after the earthquake) records similar signals, and phase changes between the before and after signals are estimated. Changes in the line-of-sight (LOS) distance between the ground and the satellite associated with the earthquake can be computed from the phase differences, after correction for satellite orbits and other confounding effects (by definition a  $2\pi$  phase change is equivalent to LOS displacement of one half of the radar wavelength). The technique is especially useful in arid regions like that around the Monte Cristo Range earthquake, where vegetation cover and atmospheric water vapour are minimal (vegetation can corrupt the phase measurement via decorrelation, while water vapour slows the microwave signal by variable amounts, changing the LOS measurement). Massonnet and Feigl (1998), Bamler and Hartl (1998), Hanssen (2001) and Simons and Rosen (2007) provide thorough reviews.

Since its initial demonstration a number of important refinements to the InSAR technique have been made. In vegetated areas, techniques that focus on strong radar scatterers within the scene can be used to overcome the decorrelation problem (e.g. Ferretti *et al.* 2001, 2011). For crustal deformation problems where the three-dimensional displacement vector is useful, several techniques have been developed to overcome the limitations of the scalar LOS measurement. For example, if both ascending and descending passes are available, the quasi east-west and up-down components of deformation can be derived. Vector information can also be obtained from

range changes from different view directions and pixel offsets in the SAR image, depending on the magnitude and orientation of deformation (Fialko *et al.* 2001, 2005; Wright *et al.* 2004). A technique called multi-aperture InSAR, exploiting changes in the Doppler history of the reflected SAR signal, has also been used (Bechor and Zebker 2006). Hu *et al.* (2014) review the various techniques available to derive three-dimensional displacements with the InSAR technique. In this study we use ascending and descending passes and the methods of Hu *et al.* (2012) and Xu *et al.* (2018) to derive the two-component data.

We used data from the European Space Agency's Sentinel-1 satellites, providing coverage several days before and after the earthquake (Table 2). The Sentinel-1 radar system consists of two satellites in identical near-polar orbits with a 12 day repeat cycle. The two satellites are separated in their orbit plane by  $180^\circ$ , meaning that each point on the ground is imaged every 6 days with identical imaging geometry (optimal for interferometry) and every three days with either an ascending or descending orbit. Both satellites transmit the same C-band signal (5.4 GHz frequency, 5.5 cm wavelength).

Figure 6 shows the ascending and descending interferograms from the Sentinel-1 satellites for the Monte Cristo Range earthquake. Note that since the second satellite pass is 2 days after the earthquake (Table 2),

**Table 2.** Information of SAR images used in geodetic modelling.

SAR data list				
Satellite	Path	Frame	Flight Direction	Acquisition Time
Sentinel-1A	71	465	Descending	20/5/11
Sentinel-1B	71	463	Descending	20/5/17
Sentinel-1A	64	119	Ascending	20/5/11
Sentinel-1B	64	118	Ascending	20/5/17
Sentinel-1B	64	123	Ascending	20/5/17

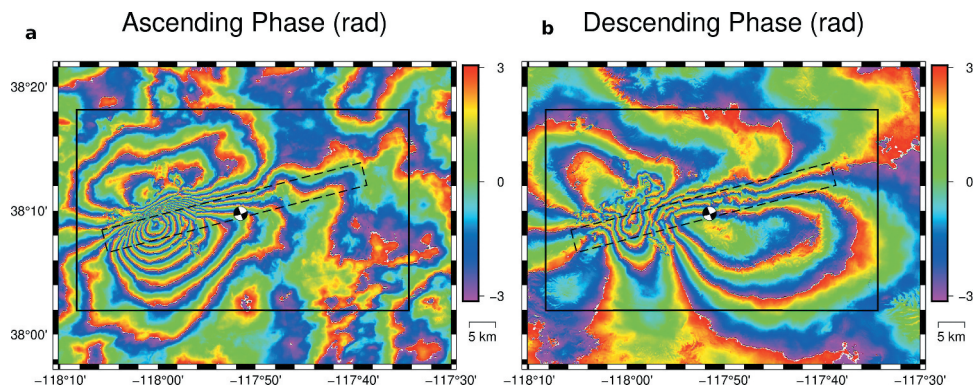


**Figure 6.** Interferograms from satellite images listed on Table 2 visualized using GMTSAR (Sandwell *et al.* 2011a, 2011b). (a) and (b) represent ascending and descending flight directions, respectively. Beachball indicates the location and focal mechanism (from USGS) of the Monte Cristo Range earthquake. Extent of Figure is indicated by the solid black box. Projected single-fault segment is shown in dashed rectangle.

the resulting LOS displacement includes not only the co-seismic offset but a variety of post-seismic effects as well. These could include a small amount of continued slip on the fault (after-slip), poro-elastic effects from water in the uppermost crust responding to earthquake-induced stress changes, and viscous relaxation in ductile lower crust and uppermost mantle. Data from continuous GPS stations near the event suggest that the cumulative effects of these various process within three months of the earthquake are less than 5% of the co-seismic offset (Hammond *et al.* 2021). This is consistent with the seismic data, which show minimal moment release via aftershocks in the immediate post-seismic period.

## 6. Deformation modelling

### 6.1. Single fault segment model

Given detailed measurements of surface deformation from the earthquake, it is possible to invert the data for the pattern of slip at depth. We assume in this type of modelling that the crustal material accommodating the earthquake is a homogeneous elastic solid, with a linear relationship between the earthquake slip at depth and displacements at the surface. This assumption is not strictly true for the upper ~ kilometre of the crust in many parts of the Basin and Range province, where thick sequences of alluvial sediments differ significantly in their mechanical properties from more rigid materials below. Nevertheless, and perhaps surprisingly, these simple models fit the observations quite well and yield useful information. Here we give a brief summary, with details provided in the Supplement. Barbot *et al.* (2009b) give an example where the layered, non-homogeneous nature of the upper crust is explicitly considered.

Okada (1985) introduced an analytical expression relating a source of deformation in an elastic half-space to surface deformation. This solution has many applications in Earth science, including the study of earthquake co-seismic and post-seismic deformations (e.g. Barbot *et al.* 2009a), inter-seismic coupling (e.g. Ader *et al.* 2012), magma intrusion (e.g. Jousset *et al.* 2003), fluid injection and resource extraction (e.g. Karegar *et al.* 2015; Deng *et al.* 2020) and water reservoir changes (e.g. Shi *et al.* 2013). Input parameters for the Okada model include constants describing the elastic properties of the medium, the location of the surface observation point, and, for faulting studies, the depth, dip, length and width of the fault plane as well as the three components of the fault slip (strike-slip, dip-slip and tensile). Model outputs are surface displacements ( $x$ ,  $y$  and  $z$  components) and their spatial derivatives.

Here we use this model and the InSAR LOS displacement data to invert for fault motions at depth. The descending and ascending SAR imagery allows creations of interferograms that indicate co-seismic displacements. To reduce the effects of aftershocks and post-seismic motion, satellite image pairs were chosen with the shortest possible time spanning the earthquake. Two main interferograms are made, using descending and ascending data of May 11 and May 17 with 6-day separation (Table 2). Pre-processing, co-registration, interferogram creation, unwrapping and geocoding are done using the ISCE2 software (Rosen *et al.* 2012). Figure 7 shows the LOS displacement, reflecting the steps of phase unwrapping and geocoding. Positive values in the LOS map indicate motion towards the satellite. LOS displacement from near-polar orbiting satellites is mostly sensitive to east-west and up-down components. The difficulty in resolving the north-south component comes from the absence of an appropriate viewing geometry

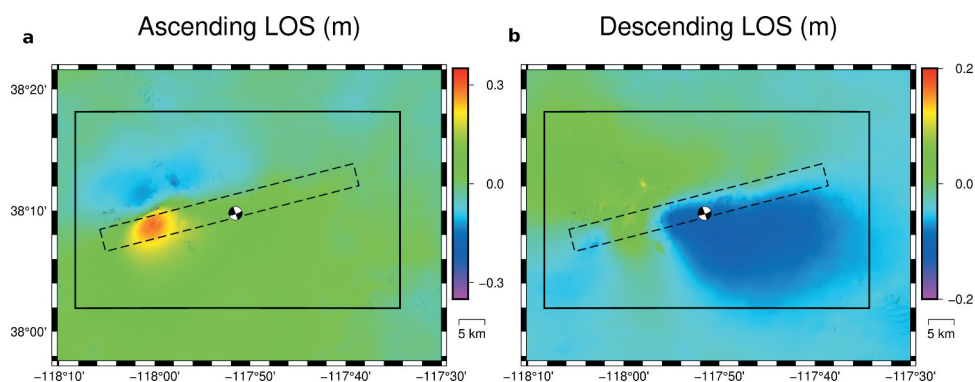


**Figure 7.** LOS displacement maps from ascending (a) and descending (b) images visualized using GMTSAR (Sandwell *et al.* 2011a, 2011b). Values are in metres (m). Beachball (from USGS) indicates the Monte Cristo Range earthquake. Extent of Figure is indicated by the solid black box. Projected single-fault segment is shown in dashed rectangle.

(Wright *et al.* 2004). The  $x$ ,  $y$  and  $z$  surface displacement components are converted to LOS displacement using the satellite incidence and heading angles, following Hu *et al.* (2012) and Xu *et al.* (2018).

To reduce the computational burden, it is useful to recognize that most of the InSAR points are spatially correlated (do not provide unique information), especially points far from the earthquake. Hence there is no need to use all points displayed in the LOS displacement figure to model slip at depth. We therefore down-sample the points using a technique called quadtree sampling (Jónsson *et al.* 2002). This reduces the number of points that are used for inversion from several million to several thousand or fewer. Figure 8 shows the resulting model, assuming all fault motion is restricted to a single fault segment. Details on the data inversion and modelling procedures are presented in the Supplement.

The moment magnitude of the earthquake can be calculated from the modelled geodetic data by summing the total motion of each patch over the slip area, assuming a value for rigidity. For our one fault segment model we obtain a geodetic moment magnitude of  $M_w$  6.61, comparable to the seismic estimate (Table 3). Most moment release occurs near  $\sim 11$  km depth and west of the mainshock epicentre.

A forward simulation is performed using the fault parameters and slip of each patch derived from the inversion to calculate the simulated LOS displacement at the surface. The residual map (the difference between the observed and simulated LOS) is one measure of model robustness and is calculated separately for ascending and descending data (Figure 9).

## 6.2. Multi-plane models

The distribution of aftershocks suggests the presence of at least two different east-northeast trending faults (Figure S4). These two left-lateral, strike-slip segments appear to have slightly different strike angles and are offset by a few kilometres. We tested whether a two-segment model fits the data significantly better than our simple, one-segment model. The maximum slip in this model occurred 1.43 m at depth  $\sim 10$  km, and 0.24 m at depth  $\sim 6$  km for west and east segment, respectively (Look at Figure S5 on supplement). A complete description for the two-segment solution is provided in the Supplement.

Since the eastern sinistral fault terminates near the southern end of the NNW-SSE trending Petrified Springs fault zone, we also implemented a three-segment

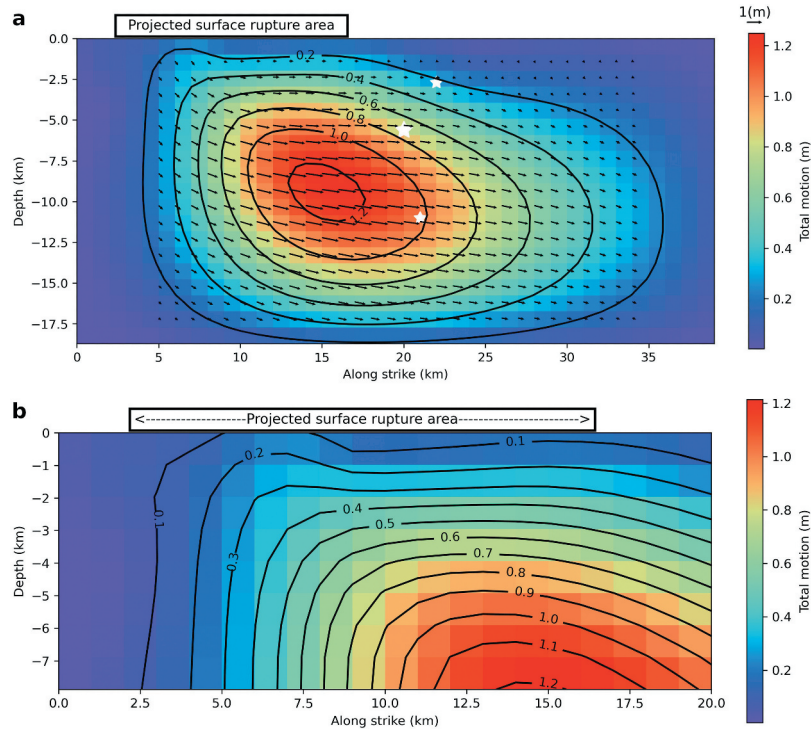


**Figure 8.** (a) Inverted slip distribution based on the single fault segment model. The deeper and shallower stars indicate the Monte Cristo Range hypocentre from the USGS and NSL locations, respectively. The large star shows the relocated hypocentre. Horizontal box represents the projected surface slip zone according to Koehler *et al.* (2021). Maximum displacement occurred at  $\sim 11$  km depth. (b) Zoomed in version of (a) focusing on the shallow western quadrant, for comparison to the region of surface rupture.



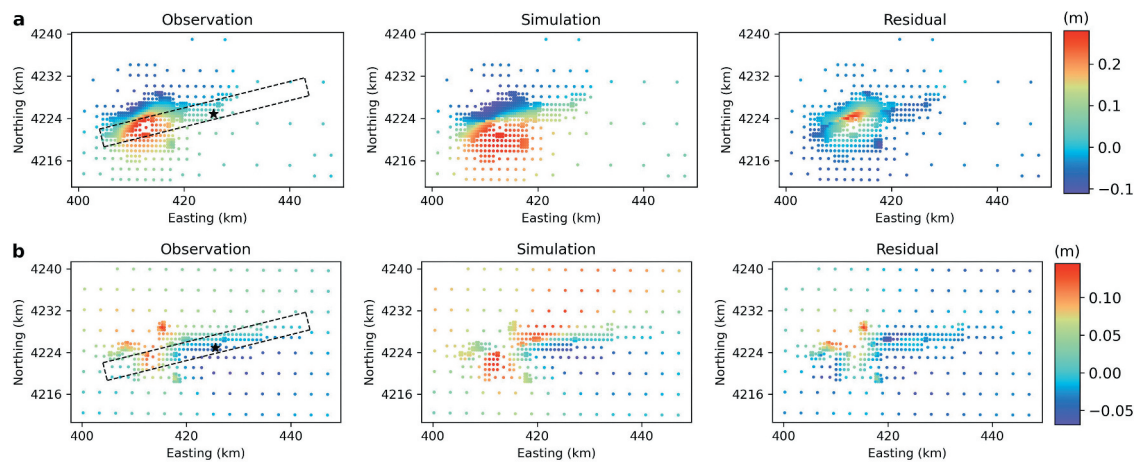


**Figure 9.** Observation, simulation and residual maps for ascending (a) and descending (b) data with down-sampled data points shown with coloured dots. Projected single-fault shown in dashed rectangle. Star represents the USGS epicentre. Note that the map is zoomed into in the fault area.

**Table 3.** Geodetic and seismic moment magnitude of each solution. See Supplement for 2-segment and 3-segment solutions. \* means value is calculated.

Solution	Moment ( $M_0$ ) [ $N.m$ ]	Moment Magnitude ( $M_w$ )
1-Segment	$9.43 \times 10^{18}$	6.61
2-Segment	$7.23 \times 10^{18}$	6.54
3-Segment	$7.96 \times 10^{18}$	6.56
USGS seismic solution	$6.77 \times 10^{18}$	6.52*
Hammond <i>et al.</i> (2021)	$4.62 \times 10^{18}$ *	6.41

model. The third segment consists of the southern Petrified Springs faults where some of the eastern aftershocks likely occurred. This eastern segment has right-lateral strike-slip with considerable normal motion, consistent with west-directed block motion. The maximum slip occurred 1.47 m at depth  $\sim 10$  km, 0.31 m at depth  $\sim 6$  km, and 0.2 m at depth  $\sim 16$  km, for west, middle and east segments, respectively (Look at Figure S7 on supplement). A detailed description of the three-segment solution is also provided in the Supplement.

Additional fault planes could be added to these three and perhaps improve data misfit, but at some point, the small misfit improvements do not justify adding free parameters (i.e. multiple fault planes). Statistical tests such as the F-test, or common sense, can guide such modelling decisions. Zheng *et al.* (2020) provide further discussion.

## 7. Discussion

Figure 8(a) shows a simple (one fault plane) model fit to the ascending and descending data. While we know the rupture was considerably more complex, this basic model illustrates three important points. First, the maximum slip ( $\sim 1.2$  metres, at 11 km depth) is much greater than the surface slip

observations, which are mostly less than 20 cm of left-lateral motion and no more than  $\sim 6$  cm of vertical offset down to northwest (Dee *et al.* 2021; Koehler *et al.* 2021). Second, the location where modelled slip reaches the surface closely coincides with the location of the mapped surface offsets (Figure 8(b)) (Koehler *et al.* 2021). This point is well west of the earthquake epicentre (surface projection of where the rupture started) implying some directionality to the rupture process; note that rupture likely propagated both east and west from the epicentre. West of the epicentre, the maximum normal displacement is  $\sim 20$  cm and reaches close to the surface. In addition, the part of the fault plane east of the epicentre shows less dip-slip motion (up to  $\sim 15$  cm) compared to the western portion. Third, maximum slip occurred at relatively shallow depth ( $\sim 11$  km), while most aftershocks occurred above this depth (Figures 8 and 10).

The depth distribution of seismicity is an important parameter, useful in formulating and testing models for the physics of earthquake rupture and friction conditions at depth. One such model (the rate-state friction model) holds that earthquake rupture will occur in regions that are velocity-weakening and hence unstable with respect to slip (i.e. friction decreases as velocity increases) (Dietrich, 1979, 1987; Ruina 1983; Tse and Rice 1986; Chester 1995; Marone 1998). Areas of the crust that are velocity-strengthening are considered stable with respect to slip and hence unlikely to generate earthquakes. Areas of the crust that exhibit intermediate or variable frictional properties are termed conditionally stable. While earthquake rupture will not initiate in these areas, their frictional properties can change abruptly as a result of stress changes associated

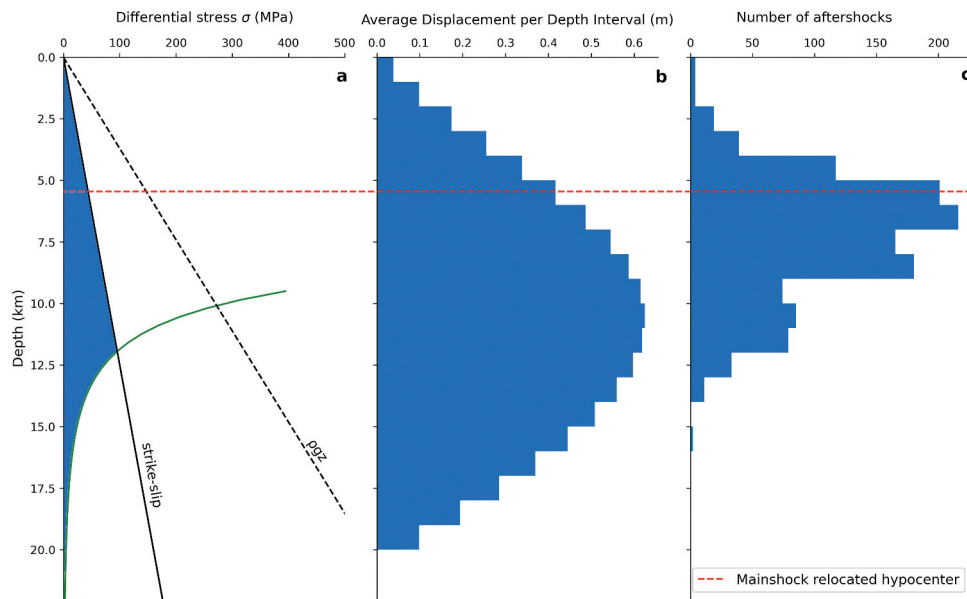


**Figure 10.** Various estimates of the brittle-ductile transition: (a) Calculated crustal strength. Brittle-ductile transition defined by the intersection of the brittle strength (strike-slip line) and the lab-generated curve for ductile quartz (green curve). See supplement for more information. (b) Average displacement per 1 km depth interval from geodetic modelling. (c) Number of aftershocks per 1 km interval. Dashed red line indicates mainshock relocated hypocentre.

with the earthquake, and they can experience earthquake-related motion (e.g. Kuna *et al.* 2019 for a model of slip in conditionally stable mantle lithosphere during oceanic strike-slip faulting).

With respect to Figure 8, if we arbitrarily define the velocity-weakening zone to be the depth range where slip is at least 50% of the maximum value, we can see that the region between about 3 km and 17 km meets this criterion; regions deeper than about 17 km would be considered velocity-strengthening. Note however that due to the well-known decrease in resolution with depth associated with surface geodetic data, this lower limit is poorly defined. In fact, a model that constrains modelled slip to the region where aftershocks occur, above 15 km, fits the InSAR data nearly as well. The region between 3 km depth and the surface is conditionally stable using the 50% of maximum slip criterion.

One problem with the rate-state friction model is that there are number of factors potentially controlling frictional behaviour. These include mineralogy, grain size, damage zone width from past earthquakes, pore fluid pressure, and temperature. Most of these are poorly constrained for the depth range where maximum slip occurs. Hence it is difficult to test the model directly by comparing our results on the depth range of seismicity to other potentially significant parameters. One exception is temperature, which can be estimated from surface heat flow and knowledge of the thermal conductivity of crustal rocks. The Basin and Range

province is characterized by relatively high heat flow, and the implied relatively high temperatures at depth may influence frictional conditions there, either directly, or indirectly, e.g. by influencing permeability, pore fluid pressure or other parameters. One way to evaluate the role of temperature is to use it to calculate the depth of the brittle-ductile transition, an important parameter in structural geology, geodesy, and seismology. Briefly, crustal strength is believed to reach a maximum in the middle crust, at a point (depth) where frictionally modulated brittle strength gives way to thermally modulated ductile strength. The maximum slip zones of large earthquakes tend to occur in or near this region, although most authors now consider the maximum strength estimated by this model to be too high, modulated instead by cataclastic, solution transfer or other processes (e.g. Chester 1995). The depth of the transition may nevertheless be important and can be estimated accurately from the intersection of frictional strength in the upper crust, calculated from theoretical considerations, and laboratory-based estimates of the ductile strength of common minerals in continental crust such as quartz. Figure 10 shows the results of this calculation, using a thermal gradient representative for this part of the Basin and Range. Note the close correspondence between the depth of the brittle-ductile transition here (12 km) and the depth of maximum slip estimated by the InSAR model (11 km). A full description of the brittle-ductile transition and how it is estimated is given in the Supplement.

The Monte Cristo Range earthquake provides two important lessons in terms of seismic hazard. Both apply to the numerous seismogenic faults of the Walker Lane and Eastern California shear zone. The first is related to the observation that mapped surface offsets are much smaller than the maximum slip at depth. Observations of shallow slip deficit are common in immature strike-slip faults and have been ascribed to distributed deformation in the upper few kilometres, mainly during the interseismic period (Fialko *et al.* 2005). If this pattern persists over many seismic cycles, it suggests that geological estimates of fault slip rate, an important aspect of seismic hazard assessment, may underestimate the true slip rate of a fault, at least for certain classes of fault (see also Xie *et al.* 2019). As of this writing (more than one year after the event), post-seismic slip does not appear to have made up the difference. GPS data from a continuous station closest to the epicentre (ID: MONT) shows only modest post-seismic motion, ending within a month of the main shock. Preliminary InSAR analysis also shows about ~10 cm post-seismic motion on the fault plane, up to a month after the main shock, much less than required to make up the shallow slip deficit. We hope to do a future study on the afterslip pattern for this earthquake.

The second lesson has to do with the relation between mapped surface faults versus the full spectrum of seismogenic faults (faults capable of generating an earthquake). The Monte Cristo Range earthquake ruptured an upper crustal section in western Nevada that included an area with no mapped surface faults. Thus, it may have ruptured previously intact rock, or reactivated previously faulted rocks with no recent history of faulting (last few hundreds of thousands of years or longer). This is important from a seismic hazard standpoint, since it makes earthquake forecasting and mitigation more challenging. For well-developed faults such as the San Andreas fault, seismic hazard maps can be developed with reasonably high levels of confidence. This is more challenging in seismically active areas such as the Walker Lane and ECSZ with their complex mosaic of surface faults. This may reflect the immaturity of this active deformation zone, where faulting is young (the current deformation regime likely started or accelerated sometime after 5 Ma) and where cumulative displacement on most faults is no more than a few km (Faulds *et al.* 2005; Dixon and Xie 2018; Xie *et al.* 2019). Wesnousky (1988, 2005a, 2005b) and Dolan and Haravitch (2014) emphasize the importance of total fault offset in defining faulting and earthquake behaviour. As offset increases over many seismic cycles, faults tend to lengthen and simplify, perhaps via friction reduction. Goumelen *et al.* (2011) present one model for this. Our understanding of this process is complicated if fault reactivation dominates – for such faults,

does the earlier phase of offset ‘count’ in terms of assessing maturity, or does fault healing nullify earlier friction reductions? With its well-recorded seismic and geodetic data, and good, well-mapped surface exposures, the Monte Cristo Range earthquake presents an exciting opportunity to test these and other models of fault evolution.

## 8. Educational aspects

There are many ways that the large amount of information resulting from the Monte Cristo Range earthquake and its aftershocks can be used for teaching, from introductory and beginning undergraduates to graduate students. It is important to adjust presentations to the knowledge base of the students.

For students in an introductory geology class, the Monte Cristo Range earthquake can be used to teach about the relationship between plate tectonics and earthquakes. A short (~5 minute) video produced by the UT-Dallas group can be used ([How did the Nevada's 2020 Earthquake happen?](#)). A brief introduction into the ways that an earthquake like this can be studied today can be presented, with explanations about foreshocks, mainshocks, and aftershocks. Introductory material could take 20–30 minutes to present, including showing the video. Such a presentation could also be adapted for the general public.

For upper division students in a structural geology, tectonics or neotectonics class, the introductory material can be supplemented by going into greater detail about the tectonics of transform plate margins and what the Walker Lane and the Mina Deflection reveal about this. The Monte Cristo Range earthquake can also be used to introduce upper division geoscience majors to modern ways of studying an earthquake. These students are ready to learn how combining information from ground rupture, locating and measuring energy release, understanding the significance of focal mechanisms, and understanding the results from GPS, InSAR, and numerical deformation modelling can lead to better understanding of this and other earthquakes. They are ready and interested to learn more about earthquakes and faulting and how earthquake magnitude and focal depth are likely to be manifested in ground rupture, displacement, and seismic hazard. Exploring these topics might take up one or two class periods. This audience will clearly benefit from reading this paper.

For graduate students, there are a number of ways to use the multiple datasets about the Monte Cristo Range earthquake summarized here, depending on the focus of the class. A general class in Tectonics could present this material in a way that is similar to that suggested for an upper division class, whereas more advanced classes in



neotectonics, seismology, or geodesy may want to spend more time on individual datasets and modelling exercises. We hope the graduate student audience will benefit from reading this paper, especially the detailed information in the Supplement. Codes and example data are provided here: <https://github.com/TahaSadeghi93/fault>.

## 9. Conclusions

1. The 15 May 2020 M 6.5 Monte Cristo Range, Nevada earthquake was a complex event rupturing faults with no apparent surface break or previously unfaulted crust within the Mina Deflection of the Walker Lane deformation belt.

2. The main rupture exhibited left-lateral motion on an east-northeast – west-southwest striking fault, but right-lateral and normal faulting components were also observed on subsidiary faults.

3. The complex rupture of this event may be characteristic of immature faults, i.e. faults with less than a few km of displacement that are less than a few million years old or were re-activated a few million years ago or less.

4. A simple one-segment fault model for the InSAR data provides useful information, demonstrating relatively shallow rupture, with maximum slip at a depth of ~11 km. The model also predicts surface slip in the location and with offset amounts that are in good agreement with surface observations.

5. Multi-segment fault models with improved fit can be constructed from the InSAR data that are consistent with the aftershock distribution. A two-segment model has two sub-parallel east-northeast – west-southwest striking left-lateral fault planes. A three-segment model includes a third fault plane striking north-northwest exhibiting right-lateral slip but with significant dip-slip motion, consistent with expectations for conjugate fault motion.

6. The earthquake and the multiple resulting datasets provide new opportunities for teaching lower division undergraduate, upper division undergraduate, and graduate students, and new research opportunities related to seismic hazard in new or rapidly evolving crustal deformation zones.

## Acknowledgments

We thank two anonymous reviewers whose comments greatly improved the manuscript. TSC was partially supported by a NASA grant 80NSSC20K0490 to THD. JB was partially supported by USGS grant G21AP10337. This is UTD Geosciences

contribution 1677. We would like to acknowledge the generous support from The Miles Foundation (<https://www.milesfdn.org/grantee-stories/2018/4/4/university-of-texas-at-dallas>) and the Ellison Miles Center for Geological Field Studies at the University of Texas at Dallas.

## Disclosure statement

No potential conflict of interest was reported by the author(s).

## Funding

This work was supported by the National Aeronautics and Space Administration [80NSSC20K0490]; U.S. Geological Survey [G21AP10337].

## ORCID

Taha Sadeghi Chorsi  <http://orcid.org/0000-0001-9052-9597>  
 Jochen Braunmiller  <http://orcid.org/0000-0002-8541-6560>  
 Fanghui Deng  <http://orcid.org/0000-0001-7545-2165>  
 Nicholas Mueller  <http://orcid.org/0000-0002-2112-3144>  
 Scott Kerstetter  <http://orcid.org/0000-0001-6242-3314>  
 Robert J. Stern  <http://orcid.org/0000-0002-8083-4632>  
 Timothy H. Dixon  <http://orcid.org/0000-0002-5127-0583>

## References

- Abe, K., 1981, Magnitudes of large shallow earthquakes from 1904 to 1980: *Physics of the Earth and Planetary Interiors*, v. 27, p. 72–92. doi:10.1016/0031-9201(81)90088-1
- Ader, T., Avouac, J.P., Liu-Zeng, J., Lyon-Caen, H., Bollinger, L., Galetzka, J., ... Flouzat, M., 2012, Convergence rate across the Nepal Himalaya and interseismic coupling on the Main Himalayan Thrust: Implications for seismic hazard: *Journal of Geophysical Research: Solid Earth*, v. 117, p. B4. doi:10.1029/2011JB009071
- Albers, J.P., and Stewart, J.H., 1972, Geology and mineral deposits of Esmeralda County, Nevada: *Nevada Bureau of Mines and Geology Bulletin*, v. 78, p. 80.
- Argus, D.F., and Gordon, R.G., 1991, Current Sierra Nevada–North America motion from very long baseline interferometry: Implications for the kinematics of the western United States: *Geology*, v. 19, no. 11, p. 1085–1088. doi:10.1130/0091-7613(1991)019<1085:CSNNAM>2.3.CO;2
- Bachman, S.B., 1978, Pliocene–Pleistocene break-up of the Sierra Nevada–White-Inyo Mountains block and formation of Owens Valley: *Geology*, v. 6, no. 8, p. 461–463. doi:10.1130/0091-7613(1978)6<461:PBOTSN>2.0.CO;2
- Bamler, R., and Hartl, P., 1998, Synthetic aperture radar interferometry: *Inverse Problems*, v. 14, no. 4, p. R1. doi:10.1088/0266-5611/14/4/001
- Barbot, S., Fialko, Y., and Bock, Y., 2009a, Postseismic deformation due to the Mw 6.0 2004 Parkfield earthquake: Stress-driven creep on a fault with spatially variable rate-and-state friction parameters: *Journal of Geophysical Research: Solid Earth*, v. 114, p. B7. doi:10.1029/2008JB005748

- Barbot, S., Fialko, Y., and Sandwell, D., 2009b, Three-dimensional models of elastostatic deformation in heterogeneous media, with applications to the Eastern California Shear Zone: *Geophysical Journal International*, v. 179, no. 1, p. 500–520. doi:10.1111/j.1365-246X.2009.04194.x
- Barrientos, S.E., Stein, R.S., and Ward, S.N., 1987, Comparison of the 1959 Hebgen Lake, Montana and the 1983 Borah Peak, Idaho, earthquakes from geodetic observations: *Bulletin of the Seismological Society of America*, v. 77, no. 3, p. 784–808. doi:10.1785/BSSA0770030784
- Beanland, S., and Clark, M.M., 1994, The Owens Valley fault zone, eastern California, and surface faulting associated with the 1872 earthquake (No. 1982). US Geological Survey. 10.3133/b1982
- Bechor, N.B., and Zebker, H.A., 2006, Measuring two-dimensional movements using a single InSAR pair: *Geophysical Research Letters*, v. 33, p. 16. doi:10.1029/2006GL026883
- Bell, J.W., dePolo, C.M., Ramelli, A.R., Sarna-Wojcicki, A.M., and Meyer, C.E., 1999, Surface faulting and paleoseismic history of the 1932 Cedar Mountain earthquake area, west-central Nevada, and implications for modern tectonics of the Walker Lane: *Geological Society of America Bulletin*, v. 111, no. 6, p. 791–807. doi:10.1130/0016-7606(1999)111<0791:SFAPHO>2.3.CO;2
- Bennett, R.A., Wernicke, B.P., Niemi, N.A., Friedrich, A.M., and Davis, J.L., 2003, Contemporary strain rates in the northern Basin and Range province from GPS data: *Tectonics*, v. 22, p. 2. doi:10.1029/2001TC001355
- Bidgoli, T.S., Amir, E., Walker, J.D., Stockli, D.F., Andrew, J.E., and Caskey, S.J., 2015, Low-temperature thermochronology of the Black and Panamint mountains, Death Valley, California: Implications for geodynamic controls on Cenozoic intraplate strain: *Lithosphere*, v. 7, no. 4, p. 473–480. doi:10.1130/L406.1
- Bock, Y., and Melgar, D., 2016, Physical applications of GPS geodesy: A review: *Reports on Progress in Physics*, v. 79, no. 10, p. 106801. doi:10.1088/0034-4885/79/10/106801
- Caskey, S.J., Wesnousky, S.G., Zhang, P., and Slemmons, D.B., 1996, Surface faulting of the 1954 Fairview Peak (MS 7.2) and Dixie Valley (MS 6.8) earthquakes, central Nevada: *Bulletin of the Seismological Society of America*, v. 86, no. 3, p. 761–787. doi:10.1785/BSSA0860030761
- Chester, F.M., 1995, A rheologic model for wet crust applied to strike-slip faults: *Journal of Geophysical Research: Solid Earth*, v. 100, no. B7, p. 13033–13044. doi:10.1029/95JB00313
- Dee, S., Koehler, R.D., Elliott, A.J., Hatem, A.E., Pickering, A., Pierce, I., Zachariasen, J., 2021, Surface rupture map of the 2020 M 6.5 Monte Cristo range earthquake, Esmeralda and Mineral counties, Nevada (No. 190). Reno, University of Nevada.
- Deng, F., Dixon, T.H., and Xie, S., 2020, Surface deformation and induced seismicity due to fluid injection and oil and gas extraction in western Texas: *Journal of Geophysical Research: Solid Earth*, v. 125, no. 5, p. e2019JB018962. doi:10.1029/2019JB018962
- Dickinson, W.R., 2002, The Basin and Range Province as a composite extensional domain: *International Geology Review*, v. 44, no. 1, p. 1–38. doi:10.2747/0020-6814.44.1.1
- Dieterich, J.H., 1979, Modeling of rock friction: 1. Experimental results and constitutive equations: *Journal of Geophysical Research: Solid Earth*, v. 84, no. B5, p. 2161–2168. doi:10.1029/JB084iB05p02161
- Dieterich, J.H., 1987, Nucleation and triggering of earthquake slip: Effect of periodic stresses: *Tectonophysics*, v. 144, no. 1–3, p. 127–139. doi:10.1016/0040-1951(87)90012-6
- Dixon, T.H., 1991, An introduction to the Global Positioning System and some geological applications: *Reviews of Geophysics*, v. 29, no. 2, p. 249–276. doi:10.1029/91RG00152
- Dixon, T.H., Miller, M., Farina, F., Wang, H., and Johnson, D., 2000, Present-day motion of the Sierra Nevada block and some tectonic implications for the Basin and Range province, North American Cordillera: *Tectonics*, v. 19, no. 1, p. 1–24. doi:10.1029/1998TC001088
- Dixon, T.H., Norabuena, E., and Hotaling, L., 2003, Paleoseismology and GPS: Earthquake cycle effects and geodetic vs geologic fault slip rates in the eastern California shear zone: *Geology*, v. 31, p. 55–58. doi:10.1130/0091-7613(2003)031<0055:PAGPSE>2.0.CO;2
- Dixon, T.H., Robaudo, S., Lee, J., and Reheis, M.C., 1995, Constraints on present-day Basin and Range deformation from space geodesy: *Tectonics*, v. 14, no. 4, p. 755–772. doi:10.1029/95TC00931
- Dixon, T.H., and Xie, S., 2018, A kinematic model for the evolution of the eastern California shear zone and Garlock fault, Mojave Desert, California: *Earth and Planetary Science Letters*, v. 494, p. 60–68. doi:10.1016/j.epsl.2018.04.050
- Dokka, R.K., and Travis, C.J., 1990a, Late Cenozoic strike-slip faulting in the Mojave Desert, California: *Tectonics*, v. 9, no. 2, p. 311–340. doi:10.1029/TC009i002p00311
- Dokka, R.K., and Travis, C.J., 1990b, Role of the eastern California shear zone in accommodating Pacific-North American plate motion: *Geophysical Research Letters*, v. 17, no. 9, p. 1323–1326. doi:10.1029/GL017i009p01323
- Dolan, J.F., and Haravitch, B.D., 2014, How well do surface slip measurements track slip at depth in large strike-slip earthquakes? The importance of fault structural maturity in controlling on-fault slip versus off-fault surface deformation: *Earth and Planetary Science Letters*, v. 388, p. 38–47. doi:10.1016/j.epsl.2013.11.043
- Doser, D.I., 1986, Earthquake processes in the Rainbow Mountain-Fairview Peak-Dixie Valley, Nevada, region 1954–1959: *Journal of Geophysical Research: Solid Earth*, v. 91, no. B12, p. 12572–12586. doi:10.1029/JB091iB12p12572
- Ekström, G., Nettles, M., and Dziewoński, A.M., 2012, The global CMT project 2004–2010: Centroid-moment tensors for 13,017 earthquakes: *Physics of the Earth and Planetary Interiors*, v. 200, p. 1–9. doi:10.1016/j.pepi.2012.04.002
- Elias, E.A., 2005, Structural control of Late Miocene to Pliocene volcanic and volcanoclastic deposition during upper-plate fragmentation in the Silver Peak Extensional Complex, west-central Great Basin [M.S. thesis]: Moscow, University of Idaho, 68 p.
- Faulds, J.E., Henry, C.D., and Hinz, N.H., 2005, Kinematics of the northern Walker Lane: An incipient transform fault along the Pacific–North American plate boundary: *Geology*, v. 33, no. 6, p. 505–508. doi:10.1130/G21274.1
- Ferranti, L., Oldow, J.S., Geissman, J.W., Neil, M.M., and Cashman, P.H., 2009, Flattening strain during coordinated slip on a curved fault array, Rhodes Salt Marsh extensional basin, central Walker Lane, west-central Nevada: Late Cenozoic Structural and Evolution of the Great Basin–Sierra Nevada Transition: *Geological Society of America Special Paper*, v. 447, p. 189–214.

- Ferretti, A., Fumagalli, A., Novali, F., Prati, C., Rocca, F., and Rucci, A., 2011, A new algorithm for processing interferometric data-stacks: SqueeSAR: *IEEE Transactions on Geoscience and Remote Sensing*, v. 49, no. 9, p. 3460–3470. doi:10.1109/TGRS.2011.2124465
- Ferretti, A., Prati, C., and Rocca, F., 2001, Permanent scatterers in SAR interferometry: *IEEE Transactions on Geoscience and Remote Sensing*, v. 39, no. 1, p. 8–20. doi:10.1109/36.898661
- Fialko, Y., Sandwell, D., Simons, M., and Rosen, P., 2005, Three-dimensional deformation caused by the Bam, Iran, earthquake and the origin of shallow slip deficit: *Nature*, v. 435, no. 7040, p. 295–299. doi:10.1038/nature03425
- Fialko, Y., Simons, M., and Agnew, D., 2001, The complete (3-D) surface displacement field in the epicentral area of the 1999 Mw7.1 Hector Mine earthquake, California, from space geodetic observations: *Geophysical Research Letters*, v. 28, no. 16, p. 3063–3066. doi:10.1029/2001GL013174
- Gabriel, A.K., Goldstein, R.M., and Zebker, H.A., 1989, Mapping small elevation changes over large areas: Differential radar interferometry: *Journal of Geophysical Research: Solid Earth*, v. 94, no. B7, p. 9183–9191. doi:10.1029/JB094iB07p09183
- Gourmelen, N., Dixon, T.H., Amelung, F., and Schmalzle, G., 2011, Acceleration and evolution of faults: An example from the Hunter Mountain–Panamint Valley fault zone, Eastern California: *Earth and Planetary Science Letters*, v. 301, no. 1–2, p. 337–344. doi:10.1016/j.epsl.2010.11.016
- Hammond, W.C., Blewitt, G., and Kreemer, C., 2011, Block modeling of crustal deformation of the northern Walker Lane and Basin and Range from GPS velocities: *Journal of Geophysical Research: Solid Earth*, v. 116, no. B4. doi:10.1029/2010JB007817
- Hammond, W.C., Blewitt, G., Kreemer, C., Koehler, R.D., and Dee, S., 2021, Geodetic observation of seismic cycles before, during, and after the 2020 Monte Cristo Range, Nevada earthquake: *Seismological Society of America*, v. 92, no. 2A, p. 647–662. doi:10.1785/0220200338
- Hammond, W.C., and Thatcher, W., 2004, Contemporary tectonic deformation of the Basin and Range province, western United States: 10 years of observation with the Global Positioning System: *Journal of Geophysical Research: Solid Earth*, v. 109, no. B8. doi:10.1029/2003JB002746
- Hanssen, R.F., 2001, *Radar interferometry: Data interpretation and error analysis*, Vol. 2. Springer Science & Business Media. Kluwer Academic Publishers, Netherlands.
- Hardyman, R.F., Oldow, J.S., Raines, G.L., Lisle, R.E., Schafer, R.W., and Wilkinson, W.H., 1991, Tertiary tectonic framework and Cenozoic history of the central Walker Lane, Nevada. *In Geology and ore deposits of the Great Basin: Reno, Nevada, Geological Society of Nevada Symposium Proceedings*, Reno, Nevada. Vol.1, pp. 279–301.
- Herrmann, R.B., Benz, H., and Ammon, C.J., 2011, Monitoring the earthquake source process in North America: *Bulletin of the Seismological Society of America*, v. 101, no. 6, p. 2609–2625. doi:10.1785/0120110095
- Hodgkinson, K.M., Stein, R.S., and King, G.C., 1996b, The 1954 rainbow Mountain–Fairview Peak–Dixie Valley earthquakes: A triggered normal faulting sequence: *Journal of Geophysical Research: Solid Earth*, v. 101, no. B11, p. 25459–25471. doi:10.1029/96JB01302
- Hodgkinson, K.M., Stein, R.S., and Marshall, G., 1996a, Geometry of the 1954 Fairview Peak–Dixie Valley earthquake sequence from a joint inversion of leveling and triangulation data: *Journal of Geophysical Research: Solid Earth*, v. 101, no. B11, p. 25437–25457. doi:10.1029/96JB01643
- Hu, J., Li, Z.W., Ding, X.L., Zhu, J.J., Zhang, L., and Sun, Q., 2012, 3D coseismic displacement of 2010 Darfield, New Zealand earthquake estimated from multi-aperture InSAR and D-InSAR measurements: *Journal of Geodesy*, v. 86, no. 11, p. 1029–1041. doi:10.1007/s00190-012-0563-6
- Hu, J., Li, Z.W., Ding, X.L., Zhu, J.J., Zhang, L., and Sun, Q., 2014, Resolving three-dimensional surface displacements from InSAR measurements: A review: *Earth-Science Reviews*, v. 133, p. 1–17. doi:10.1016/j.earscirev.2014.02.005
- Jónsson, S., Zebker, H., Segall, P., and Amelung, F., 2002, Fault slip distribution of the 1999 M w 7.1 Hector Mine, California, earthquake, estimated from satellite radar and GPS measurements: *Bulletin of the Seismological Society of America*, v. 92, no. 4, p. 1377–1389. doi:10.1785/0120000922
- Jousset, P., Mori, H., and Okada, H., 2003, Elastic models for the magma intrusion associated with the 2000 eruption of Usu Volcano, Hokkaido, Japan: *Journal of Volcanology and Geothermal Research*, v. 125, no. 1–2, p. 81–106. doi:10.1016/S0377-0273(03)00090-8
- Karegar, M.A., Dixon, T.H., Malservisi, R., Yang, Q., Hossaini, S.A., and Hovorka, S.D., 2015, GPS-based monitoring of surface deformation associated with CO2 injection at an enhanced oil recovery site: *International Journal of Greenhouse Gas Control*, v. 41, p. 116–126. doi:10.1016/j.ijggc.2015.07.006
- Katopody, D.T., 2018, *Extensional and accretionary tectonics of Western North America: Examples from the Southern Walker Lane and Northwestern Washington State* [Doctoral dissertation].
- Kerstetter, S.R., 2018, *Late Oligocene to early Miocene North-South extension in the Western Great Basin* [Doctoral dissertation].
- Kirby, E., Anandakrishnan, S., Phillips, F., and Marrero, S., 2008, Late Pleistocene slip rate along the Owens Valley fault, eastern California: *Geophysical Research Letters*, v. 35, p. 1. doi:10.1029/2007GL031970
- Koehler, R.D., Dee, S., Elliott, A., Hatem, A., Pickering, A., Pierce, I., and Seitz, G., 2021, Field Response and Surface-Rupture Characteristics of the 2020 M 6.5 Monte Cristo Range Earthquake, Central Walker Lane, Nevada: *Seismological Society of America*, v. 92, no. 2A, p. 823–839. doi:10.1785/0220200371
- Kuna, V.M., Nabelek, J.L., and Braunmiller, J., 2019, Mode of slip and crust-mantle interaction at oceanic transform faults: *Nature Geoscience*, v. 12, p. 138–142. doi:10.1038/s41561-018-0287-1
- Lee, J., Spencer, J., and Owen, L., 2001, Holocene slip rates along the Owens Valley fault, California: Implications for the recent evolution of the Eastern California Shear Zone: *Geology*, v. 29, no. 9, p. 819–822. doi:10.1130/0091-7613(2001)029<0819:HSRATO>2.0.CO;2
- Lee, J., Stockli, D.F., Owen, L.A., Finkel, R.C., and Kislitsyn, R., 2009, Exhumation of the Inyo Mountains, California: Implications for the timing of extension along the western boundary of the Basin and Range Province and distribution of dextral fault slip rates across the eastern California shear zone: *Tectonics*, v. 28, p. 1. doi:10.1029/2008TC002295



- Lee, J., Stockli, D., Schroeder, J., Tincher, C., Bradley, D., Owen, L., Gosse, J., and Garwood, J., 2006, Fault slip transfer in the Eastern California Shear Zone-Walker Lane Belt, in Lee, J., ed., Geological society of America, Mammoth Lakes, CA. p. 1–26.
- Liberty, L.M., Lifton, Z.M., and Mikesell, T.D., 2021, The 31 March 2020 Mw 6.5 Stanley, Idaho, earthquake: Seismotectonic analysis and preliminar aftershock analysis, *Seis: Research Letters*, v. 92, no. 2A, p. 663–678. doi:10.1785/0220200319
- Locke, A., Billingsley, P., and Mayo, E.B., 1940, Sierra Nevada tectonic pattern: *Bulletin of the Geological Society of America*, v. 51, no. 4, p. 513–539. doi:10.1130/GSAB-51-513
- Lubetkin, L.K., and Clark, M.M., 1988, Late Quaternary activity along the Lone Pine fault, eastern California: *Geological Society of America Bulletin*, v. 100, no. 5, p. 755–766. doi:10.1130/0016-7606(1988)100<0755:LQAATL>2.3.CO;2
- Mahan, K.H., Guest, B., Wernicke, B., and Niemi, N.A., 2009, Low-temperature thermochronologic constraints on the kinematic history and spatial extent of the Eastern California shear zone: *Geosphere*, v. 5, no. 6, p. 483–495. doi:10.1130/GES00226.1
- Malservisi, R., Dixon, T.H., La Femina, P.C., and Furlong, K.P., 2003, Holocene slip rate of the Wasatch fault zone, Utah, from geodetic data: *Earthquake cycle effects: Geophysical Research Letters*, v. 30, p. 13. doi:10.1029/2003GL017408
- Marone, C., 1998, Laboratory-derived friction laws and their application to seismic faulting: *Annual Review of Earth and Planetary Sciences*, v. 26, no. 1, p. 643–696. doi:10.1146/annurev.earth.26.1.643
- Massonnet, D., and Feigl, K.L., 1998, Radar interferometry and its application to changes in the Earth's surface: *Reviews of Geophysics*, v. 36, no. 4, p. 441–500. doi:10.1029/97RG03139
- Massonnet, D., Rossi, M., Carmona, C., Adragna, F., Peltzer, G., Feigl, K., and Rabaute, T., 1993, The displacement field of the Landers earthquake mapped by radar interferometry: *Nature*, v. 364, no. 6433, p. 138–142. doi:10.1038/364138a0
- McClusky, S.C., Bjornstad, S.C., Hager, B.H., King, R.W., Meade, B. J., Miller, M.M., ... Souter, B.J., 2001, Present day kinematics of the eastern California shear zone from a geodetically constrained block model: *Geophysical Research Letters*, v. 28, no. 17, p. 3369–3372. doi:10.1029/2001GL013091
- Miller, M.M., Johnson, D.J., Dixon, T.H., and Dokka, R.K., 2001, Refined kinematics of the Eastern California shear zone from GPS observations, 1993–1998: *Journal of Geophysical Research: Solid Earth*, v. 106, no. B2, p. 2245–2263. doi:10.1029/2000JB900328
- Minster, J.B., and Jordan, T.H., 1984, Vector constraints on Quaternary deformation of the western United States east and west of the San Andreas fault.
- Minster, J.B., and Jordan, T.H., 1987, Vector constraints on western US deformation from space geodesy, neotectonics, and plate motions: *Journal of Geophysical Research: Solid Earth*, v. 92, no. B6, p. 4798–4804. doi:10.1029/JB092iB06p04798
- Mueller, N.J., 2019, Pliocene kinematic reorganization, fault geometry, basin evolution, and displacement budget along the Furnace Creek–Fish Lake Valley Fault Zone, Eastern California and Western Nevada [Doctoral dissertation].
- Murphy, J.J., Watkinson, A.J., and Oldow, J.S., 2009, Spatially partitioned transtension within the central Walker Lane, western Great Basin, USA: Application of the polar Mohr construction for finite deformation: *Geological Society of America Special Paper*, v. 447, p. 55–70.
- Okada, Y., 1985, Surface deformation due to shear and tensile faults in a half-space: *Bulletin of the Seismological Society of America*, v. 75, no. 4, p. 1135–1154. doi:10.1785/BSSA0750041135
- Oldow, J.S., 2003, Active transtensional boundary zone between the western Great Basin and Sierra Nevada block, western US Cordillera: *Geology*, v. 31, no. 12, p. 1033–1036. doi:10.1130/G19838.1
- Oldow, J.S., Aiken, C.L.V., Hare, J.L., Ferguson, J.F., and Hardyman, R.F., 2001, Active displacement transfer and differential block motion within the central Walker Lane, western Great Basin: *Geology*, v. 29, no. 1, p. 19–22. doi:10.1130/0091-7613(2001)029<0019:ADTADB>2.0.CO;2
- Oldow, J.S., and Cland, B., 2018, Late Cenozoic high-angle transtensional and low-angle detachment faults in the eastern Mina deflection, west-central Nevada (*Geological Society of Nevada Special Paper No. 65*).
- Oldow, J.S., and Craig, S.D., 1992, Late Cenozoic displacement partitioning in the northwestern Great Basin: Structure, Tectonics, and Mineralization of the Walker Lane, symposium proceedings volume: Reno, Nevada, Geological Society of Nevada. p. 17–52.
- Oldow, J.S., Elias, E.A., Ferranti, L., McClelland, W.C., McIntosh, W.C., and Cashman, P.H., 2009, Late Miocene to Pliocene synextensional deposition in fault-bounded basins within the upper plate of the western Silver Peak–Lone Mountain extensional complex, west-central Nevada: Late Cenozoic Structure and Evolution of the Great Basin–Sierra Nevada Transition: *Geological Society of America Special Paper*, v. 447, p. 275–312.
- Oldow, J.S., Geissman, J.W., and Stockli, D.F., 2008, Evolution and strain reorganization within late Neogene structural stepovers linking the central Walker Lane and northern Eastern California shear zone, western Great Basin: *International Geology Review*, v. 50, no. 3, p. 270–290. doi:10.2747/0020-6814.50.3.270
- Oldow, J.S., Katopody, D.T., Kerstetter, S.R., and Mueller, N.J., 2016, Regional setting, geometry, and structure of the northern Fish Lake Valley basin (*American Lithium Corporation Technical Report*).
- Oldow, J.S., Kohler, G., and Donelick, R.A., 1994, Late Cenozoic extensional transfer in the Walker Lane strike-slip belt, Nevada: *Geology*, v. 22, no. 7, p. 637–640. doi:10.1130/0091-7613(1994)022<0637:LCETIT>2.3.CO;2
- Reheis, M.C., and Dixon, T.H., 1996, Kinematics of the Eastern California shear zone: Evidence for slip transfer from Owens and Saline Valley fault zones to Fish Lake Valley fault zone: *Geology*, v. 24, p. 575. doi:10.1130/0091-7613(1996)024<0339:KOTECES>2.3.CO;2
- Rogers, A.M., Harmsen, S.C., Corbett, E.J., Priestley, K., and dePolo, D., 1991, The seismicity of Nevada and some adjacent parts of the Great Basin: *Neotectonics of North America*, v. 1, p. 153–184.
- Rosen, P.A., Gurrola, E., Sacco, G.F., and Zebker, H., 2012, The InSAR scientific computing environment. *In EUSAR 2012; 9th European Conference on Synthetic Aperture Radar*, VDE, Nuremberg, Germany. pp. 730–733.
- Ross, D.C., 1961, Geology and mineral deposits of Mineral County, Nevada: Nevada Bureau of Mines and Geology Bulletin, v. 58, p. 112.

- Ross, Z.E., Idini, B., Jia, Z., Stephenson, O.L., Zhong, M., Wang, X., ... Jung, J., 2019, Hierarchical interlocked orthogonal faulting in the 2019 Ridgecrest earthquake sequence: *Science*, v. 366, no. 6463, p. 346–351. doi:10.1126/science.aaz0109
- Ruhl, C.J., Morton, E.A., Bormann, J.M., Hatch-Ibarra, R., Ichinose, G., and Smith, K.D., 2021, Complex Fault Geometry of the 2020 M<sub>w</sub> 6.5 Monte Cristo Range, Nevada, Earthquake Sequence: *Seismological Society of America*, v. 92, no. 3, p. 1876–1890. doi:10.1785/0220200345
- Ruina, A., 1983, Slip instability and state variable friction laws: *Journal of Geophysical Research: Solid Earth*, v. 88, no. B12, p. 10359–10370. doi:10.1029/JB088iB12p10359
- Ryall, A., and Priestley, K., 1975, Seismicity, secular strain, and maximum magnitude in the Excelsior Mountains area, western Nevada and eastern California: *Geological Society of America Bulletin*, v. 86, p. 1585–1592. doi:10.1130/0016-7606(1975)86<1585:SSSAMM>2.0.CO;2
- Sandwell, D., Mellors, R., Tong, X., Wei, M., and Wessel, P., 2011a, GmtSAR: An insar processing system based on generic mapping tools. Retrieved from: <https://escholarship.org/uc/item/8zq2c02m>
- Sandwell, D., Mellors, R., Tong, X., Wei, M., and Wessel, P., 2011b, Open radar interferometry software for mapping surface deformation. 10.1029/2011EO280002
- Sauber, J., Thatcher, W., and Solomon, S.C., 1986, Geodetic measurement of deformation in the central Mojave Desert, California: *Journal of Geophysical Research: Solid Earth*, v. 91, no. B12, p. 12683–12693. doi:10.1029/JB091iB12p12683
- Sauber, J., Thatcher, W., Solomon, S.C., and Lisowski, M., 1994, Geodetic slip rate for the eastern California shear zone and the recurrence time of Mojave Desert earthquakes: *Nature*, v. 367, no. 6460, p. 264–266. doi:10.1038/367264a0
- Savage, J.C., Lisowski, M., and Prescott, W.H., 1990, An apparent shear zone trending north-northwest across the Mojave Desert into Owens Valley, eastern California: *Geophysical Research Letters*, v. 17, no. 12, p. 2113–2116. doi:10.1029/GL017i012p02113
- Shi, Z., Wang, G., and Liu, C., 2013, Co-seismic groundwater level changes induced by the May 12, 2008 Wenchuan earthquake in the near field: *Pure and Applied Geophysics*, v. 170, no. 11, p. 1773–1783. doi:10.1007/s00024-012-0606-1
- Sieh, K., Jones, L., Hauksson, E., Hudnut, K., Eberhart-Phillips, D., Heaton, T., ... Zachariasen, J., 1993, Near-field investigations of the Landers earthquake sequence, April to July 1992: *Science*, v. 260, no. 5105, p. 171–176. doi:10.1126/science.260.5105.171
- Simons, M., and Rosen, P.A., 2007, Interferometric synthetic aperture radar geodesy. *Treatise on Geophysics*, Elsevier, Amsterdam, 2007, 391–446. doi:10.1016/B978-0-444-52748-6.00059-6
- Speed, R.C., and Cogbill, A.H., 1979, Deep fault trough of Oligocene age, Candelaria Hills, Nevada: Summary: *Geological Society of America Bulletin*, v. 90, p. 145–148. doi:10.1130/0016-7606(1979)90<145:DFTOOA>2.0.CO;2
- Stewart, J.H., 1979, Geologic map of Miller Mountain and Columbus quadrangles, mineral and Esmeralda counties, Nevada: US Geological Survey Open-File Report, v. 79, p. 1145.
- Stewart, J.H., 1988, Tectonics of the Walker Lane belt, western Great Basin: Mesozoic and Cenozoic deformation in a shear zone, in Ernst, W.G., ed., *Metamorphism and crustal evolution of the western United States*: Englewood Cliffs: New Jersey, Prentice-Hall, p. 681–713.
- Stockli, D.F., Dumitru, T.A., McWilliams, M.O., and Farley, K.A., 2003, Cenozoic tectonic evolution of the White Mountains, California and Nevada: *Geological Society of America Bulletin*, v. 115, no. 7, p. 788–816. doi:10.1130/0016-7606(2003)115<0788:CTEOTW>2.0.CO;2
- Tse, S.T., and Rice, J.R., 1986, Crustal earthquake instability in relation to the depth variation of frictional slip properties: *Journal of Geophysical Research: Solid Earth*, v. 91, no. B9, p. 9452–9472. doi:10.1029/JB091iB09p09452
- Utsu, T., 1961, A statistical study on the occurrence of after-shocks: *Geophysical Magazine*, v. 30, p. 521–605.
- Waldhauser, F., and Ellsworth, W.L., 2000, A double-difference earthquake location algorithm: Method and application to the northern Hayward fault, California: *Bulletin of the Seismological Society of America*, v. 90, no. 6, p. 1353–1368. doi:10.1785/0120000006
- Walker, J.D., Bidgoli, T.S., Didericksen, B.D., Stockli, D.F., and Andrew, J.E., 2014, Middle Miocene to recent exhumation of the Slate Range, eastern California, and implications for the timing of extension and the transition to transtension: *Geosphere*, v. 10, no. 2, p. 276–291. doi:10.1130/GES00947.1
- Wells, D.L., and Coppersmith, K.J., 1994, New empirical relationships among magnitude, rupture length, rupture width, rupture area, and surface displacement: *Bulletin of the Seismological Society of America*, v. 84, no. 4, p. 974–1002. doi:10.1785/BSSA0840040974
- Wesnousky, S.G., 1988, Seismological and structural evolution of strike-slip faults: *Nature*, v. 335, no. 6188, p. 340–343. doi:10.1038/335340a0
- Wesnousky, S.G., 2005a, Active faulting in the Walker Lane: *Tectonics*, v. 24, p. 3. doi:10.1029/2004TC001645
- Wesnousky, S.G., 2005b, The San Andreas and Walker Lane fault systems, western North America: Transpression, transtension, cumulative slip and the structural evolution of a major transform plate boundary: *Journal of Structural Geology*, v. 27, no. 8, p. 1505–1512. doi:10.1016/j.jsg.2005.01.015
- Williams, M.C., Tréhu, A.M., and Braunmiller, J., 2011, Seismicity at the Cascadia plate boundary beneath the Oregon continental shelf: *Bulletin of the Seismological Society of America*, v. 101, no. 3, p. 940–950. doi:10.1785/0120100198
- Wright, T.J., Parsons, B.E., and Lu, Z., 2004, Toward mapping surface deformation in three dimensions using InSAR: *Geophysical Research Letters*, v. 31, p. 1. doi:10.1029/2003GL018827
- Xie, S., Gallant, E., Wetmore, P.H., Figueiredo, P.M., Owen, L.A., Rasmussen, C., ... Dixon, T.H., 2019, A new geological slip rate estimate for the Calico Fault, eastern California: Implications for geodetic versus geologic rate estimates in the Eastern California Shear Zone: *International Geology Review*, v. 61, no. 13, p. 1613–1641. doi:10.1080/00206814.2018.1531272
- Xu, G., Xu, C., and Wen, Y., 2018, Sentinel-1 observation of the 2017 Sangsefid earthquake, northeastern Iran: Rupture of a blind reverse-slip fault near the Eastern Kopeh Dagh: *Tectonophysics*, v. 731, p. 131–138. doi:10.1016/j.tecto.2018.03.009
- Zheng, A., Chen, X., and Xu, W., 2020, Present-day deformation mechanism of the northeastern Mina deflection revealed by the 2020 M<sub>w</sub> 6.5 Monte Cristo Range earthquake: *Geophysical Research Letters*, v. 47, no. 22, p. e2020GL090142. doi:10.1029/2020GL090142